PAPER • OPEN ACCESS

Multi-machine scaling laws for fuel and impurity puffing rates sufficient for detachment access: a systematic review of magnetic confinement fusion devices

To cite this article: M. Moscheni *et al* 2026 *Nucl. Fusion* **66** 026008

OPEN ACCESS
IOP Publishing | International Atomic Energy Agency
Nuclear Fusion
Nucl. Fusion **66** (2026) 026008 (24pp)
https://doi.org/10.1088/1741-4326/ae287c

Multi-machine scaling laws for fuel and impurity puffing rates sufficient for detachment access: a systematic review of magnetic confinement fusion devices

M. Moscheni[1,*], A. Herrmann[1], R. Kembleton[1], M. Kryjak[2], S. Lazerson[1], F. Levi[1], M. Siccinio[3,4], P. Staniec[1], T. Giegerich[5], C. Tantos[5] and the Gauss Fusion Team[1,a]

[1] Gauss Fusion GmbH, Parkring 29, 85748 Garching bei München, Germany
[2] United Kingdom Atomic Energy Authority, Culham Campus, Abingdon OX14 3DB, United Kingdom of Great Britain and Northern Ireland
[3] Max-Planck-Institut für Plasmaphysik, 85748 Garching bei München, Germany
[4] EUROfusion Consortium, 85748 Garching bei München, Germany
[5] Karlsruhe Institute of Technology, Hermann-von-Helmholtz-Platz 1, 76344 Eggenstein-Leopoldshafen, Germany

E-mail: matteo.moscheni@gauss-fusion.com

Received 26 September 2025, revised 12 November 2025
Accepted for publication 5 December 2025
Published 22 December 2025

Abstract

An open-source database of 457 experimental and numerical entries representing 32 machines—including tokamaks, stellarators, and linear plasma devices—is assembled. From this dataset, we derive multi-machine scaling laws that predict the fuel and impurity puffing rates sufficient to edge plasma detachment—the leading reactor-relevant solution to the challenge of plasma–wall interaction. Validation against up to 40 L- and H-mode plasmas shows agreement within a factor of 1.5 in about 50% of cases, and within a factor of 2 on average. Divertor volume alone is found to strongly correlate with the fuelling rate. Inclusion of plasma opaqueness leads to $\Gamma_{\mathrm{D}} \propto \left[n_{\mathrm{sep}}\, a\, (S_{\mathrm{div}}/V_{\mathrm{div}})^{-1.5}\right]^{1.05}$, valid across all toroidal devices. Its H-mode simplification, $\Gamma_{\mathrm{D}}^{\mathrm{HDL}} \propto 0.43\, a^{1.58}\, \lambda_q^{-0.89}$, avoids explicit dependence on n_{sep} and carries intrinsic physical meaning through the H/L density limit and the power fall-off length. The impurity seeding rate is captured by a general non-linear law, from which the Greenwald–Eich–Scarabosio (GES) simplification, $\Gamma_{\mathrm{Z}}^{\mathrm{GES}} \propto a^{1.51}\, \lambda_q^{-0.27}$, is obtained. Similar relationships are defined for stellarators, consistent with tokamak trends but still awaiting validation—an opportunity for further study. These results have immediate relevance for reactor fuel-cycle design and edge plasma modelling. More broadly, they demonstrate that physics-based 0D laws can reliably link detachment access to engineering actuators, offering practical tools for reactor design. Our laws represent macroscopic patterns across machines rather than microscopic variations within an individual device—providing the basis for our forthcoming studies aimed at extending this framework to machine-specific behaviour.

[a] See Moscheni *et al* 2025 (https://doi.org/10.1088/1741-4326/ae287c) for the Gauss Fusion Team.
[*] Author to whom any correspondence should be addressed.

Keywords: fusion reactor design, plasma–wall interaction, plasma detachment, multi-machine scaling laws, fuel puffing, impurity seeding, validation

(Some figures may appear in colour only in the online journal)

1. Introduction

The past few decades witnessed a speciation of magnetic confinement fusion devices culminating in the coexistence of designs for conventional [1], spherical [2], high-field tokamaks [3] and stellarators [4] as possible candidates to harness nuclear fusion.

Common denominator is the open issue of the edge plasma and its interactions with the divertor plasma-facing components [5–8]—where the edge plasma must be tuned such that realistic engineering can simultaneously satisfy tight constraints of power and particle exhaust (few tens of MW $\times$ m^{-2} and hundreds of Pa $\times$ m^3 $\times$ s^{-1}, respectively [9, 10]), and divertor survival ($\sim$5 year lifetime [11]). The most widely accepted solution is the detached edge plasma scenario [12, 13], a highly-dissipative state that cools the plasma to protect the divertor materials, and which is established by puffing gaseous fuel and seeded impurities—focus of the present study. In pilot plants, these injection rates will likely be controlled in real-time to maintain the detached state [14–16], whereby keeping the plasma-divertor interaction suppressed during the plasma discharge.

Quantifying the required fuel puffing rate and impurity seeding ratio presents one of the most significant challenges in the design of the tritium fuel cycle (TFC [17, 18]) associated to a magnetic confinement fusion device. Designing a TFC with an under-estimated puffing rate would preclude a safe detached operation altogether. However, over-estimating for a 'worst case scenario' with the highest possible feed rate requirements and later relying on a reduced operation of the TFC is also impractical. This would lead to an oversized plant, requiring unnecessary extra tritium inventory (with regulator and safety considerations), as well as incurring additional capital and operational costs. It may also lead to sub-optimal technology selections. Thus, potential puffing values spanning several orders of magnitude can not be realistically used as a starting point for a reactor design and a more reliable foundation must be established.

The task of estimating puffing rates compatible with a robust detached operation is traditionally tackled via state-of-the-art suites dedicated to 2D edge plasma simulations (e.g. SOLPS-ITER [19, 20], SOLEDGE3X [21] and EDGE2D-EIRENE [22, 23]), uniquely predisposed to model the multi-species transport from the puffing injection valve to the divertor. Multi-parameter scans with such tools ultimately bound, among many others, the admissible puffing rates for fuel and impurities [24–27].

Comprising in excess of 125 SOLPS-ITER simulations for a single operating point—each worth up to a month of wall clock time [28], the ITER edge plasma database [29] is among the most comprehensive ones ever assembled, and is yet constantly expanded [28]. Despite its recognised success, this approach is hardly replicable for other tokamaks, notwithstanding the rapid pace pick-up of stellarator designs [30, 31] and their need of 3D simulations [32].

Other authors acknowledged the above. Some distilled regression laws—but specific to a single device, not accounting for detachment [33, 34] or impurities [35, 36]. Others created promising neural network surrogates [37, 38], though at the cost of losing physical interpretability and, for the time being, only applicable for certain configurations. And still others successfully constructed 0.5D physical models [10, 39–45] which provide valuable insight but, nonetheless, necessitate of assumptions, estimates and understanding beyond those needed for 0D scaling laws.

Here we follow the recommendation of Lore *et al* [28]: '[...] the relationship between the actuators and effective sorting variables should be explored'—but we apply it at large. Complementing the afore-mentioned studies, the present work scrutinises the puffing rates across devices via a human-driven systematic review of published data for stably detached edge plasmas to obtain widely-applicable 0D laws.

The paper is organised as follows. Section 2 illustrates the features of the database employed in the analyses, the conventions adopted and the assessment strategy. Section 3 presents the results of the study—scaling law derivation and validation. Section 4 discusses this work compared to the existing knowledge, its interpretation and caveats. Practical examples applied to reactor concepts are also provided, before drawing the conclusions in section 5.

2. Methods

2.1. Database overview

The database here considered (available at [46]) groups experimental and numerical data from 20 conventional tokamaks ('CTKs', e.g. HL-2A [47], JFT-2M [48]), 5 spherical tokamaks ('STKs', e.g. NSTX [49]), 2 high-field tokamaks ('HFTKs', e.g. SPARC [50]) and 3 stellarators ('STLs', e.g. LHD [51]). With the addition of 5 linear plasma devices ('LPDs', e.g. Magnum-PSI [52], MAP-II [53]), all the magnetic confinement fusion devices are encompassed. Machine IDs and references are reported in appendix.

The salient features of the database are summarised in table 1 and further detailed in section 2.2. Overall, 5 orders of magnitude worth of machine volume, and 3 of power, are spanned throughout the 32 different devices expounded in 124 scientific publications. Each of the 193 entries from 7 different simulation tools [19, 21, 22, 54–57] and each of the

Table 1. Main variables accompanied by their units and their minimum (Min.) and maximum (Max.) values in the database for the cases past (DOD>1, training set) and at (DOD = 1, validation set) the detachment onset (see text for details).

		Training set (DOD>1)		Validation set (DOD = 1)	
Variable	Units	Min.	Max.	Min.	Max.
n. data	—	—	412	16	45
R_0	m	0.36	9	0.7	8.9
a	m	0.16	2.9	0.25	2.9
A	—	1.2	12	1.4	6.2
V_p	m^3	6.5×10^{-1}	2.5×10^{3}	1.6×10^{0}	2.5×10^{3}
V_div	m^3	3.8×10^{-3}	4.8×10^{2}	6.9×10^{-2}	1.5×10^{2}
n. L-modes	—	—	80	—	20
n. H-modes	—	—	294	—	21
P_sep	MW	1.2×10^{-1}	2.0×10^{2}	2.1×10^{-1}	1.7×10^{2}
$\lambda_q^\mathrm{E}\times f^\mathrm{S}$	mm	0.25	14	0.25	27
n^G	m^{-3}	3.0×10^{19}	8.5×10^{20}	3.0×10^{19}	6.7×10^{20}
n^Su	m^{-3}	4.3×10^{19}	1.5×10^{20}	—	—
n_sep	m^{-3}	3.5×10^{18}	2.0×10^{20}	3.3×10^{18}	1.2×10^{20}
$n_\mathrm{sep}\times a$	m^{-2}	2.0×10^{18}	2.0×10^{20}	1.7×10^{18}	1.2×10^{20}
Γ_D	$\mathrm{el}\times\mathrm{s}^{-1}$	4.2×10^{19}	2.5×10^{24}	1.0×10^{20}	5.0×10^{23}
Γ_Z	$\mathrm{el}\times\mathrm{s}^{-1}$	2.2×10^{19}	4.9×10^{23}	2.2×10^{19}	2.1×10^{23}
$\Gamma_\mathrm{D}/\Gamma_\mathrm{Z}$	—	4.1×10^{-3}	3.9×10^{2}	9.5×10^{-3}	4.6×10^{1}

264 experimental instances correspond to edge plasmas exhibiting stable detachment at the outer target without MARFE [58] (section 2.2.4). The database as a whole encompasses a wide range of features, including divertor geometry (open or closed divertor [59]), magnetic topology (whether linear [60], diverted double-null with [61] or single-null without [62] advanced magnetic configurations [63–65], or island divertors [66]), seeded impurity species [67], divertor material (e.g. molybdenum [68], carbon [69]), type of radiation emission (e.g. traditional or X-point radiator [70]) and puff location [24, 71]. Last but not least, transient and steady L-modes [72] and H-modes (EDA [73] and not [74]) populate the database.

2.2. Variables and conventions

2.2.1. Geometrical parameters. Nominal values of geometrical parameters (e.g. plasma elongation κ) are added where lacking in the database. The variables considered and listed in table 1 are: the machine major and minor radii, R_0 and a, respectively; the aspect ratio $A = R_0/a$; the plasma and divertor volumes, V_p and V_div, respectively. The plasma volume V_p is computed as $2\pi^2 R_0 a^2 \kappa$. The volume (V_div) and surface (S_div) of the divertor are approximated by simplistic generalisations:

$$\begin{aligned} V_\mathrm{div} &= N_\mathrm{div}\times f_\mathrm{tor}\times 2\pi R_\mathrm{div}\times(L_\mathrm{div}\times H_\mathrm{div})\ , \\ S_\mathrm{div} &= N_\mathrm{div}\times f_\mathrm{tor}\times 2\pi R_\mathrm{div}\times(L_\mathrm{div}+H_\mathrm{div})\times 2\ . \end{aligned} \tag{1}$$

In equation (1), N_div is the number of active divertors and attains a value of 2 in the stellarators considered; in tokamaks [75]: $N_\mathrm{div} = 1$ in single-null diverted plasmas, and disconnected double-nulls if featuring a power fall-off length significantly smaller than the separation of the two separatrices, i.e. $\lambda_q \ll \delta R_\mathrm{sep}$; $N_\mathrm{div} = 2$ in double-nulls and disconnected double-nulls for which $\lambda_q \gtrsim \delta R_\mathrm{sep}$. The toroidal coverage is estimated by f_tor: 50% for W7-AS' and W7-X's island divertors, and 100% otherwise. The remaining entries are defined via the yellow-shaded rectangle pictured in figure 1 (dash-dotted lines): L_div is the length of the segment connecting inner and outer strike points (red); H_div is the distance of the X-point from it (orange); R_div is the radius of the segment's mid-point (black). On average across the database[6] it holds that:

$$\begin{aligned} L_\mathrm{div} &\sim 0.76\times a\ , \\ H_\mathrm{div} &\sim 0.35\times a\ , \\ R_\mathrm{div} &\sim 2.40\times a\ , \end{aligned} \tag{2}$$

and will be used in the following. The lack of closed field lines in linear plasma devices means that neither V_p nor n_sep are defined for such devices, and V_div equals the chamber volume.

2.2.2. Physics quantities. Physics-based entries of the database (e.g. density) are left blank where not retrievable. In table 1, physics variables are:

□ The number of L- and H-mode plasmas;

[6] However, stellarators and, for instance, the WEST tokamak (section 3.1.1) violate these trends.

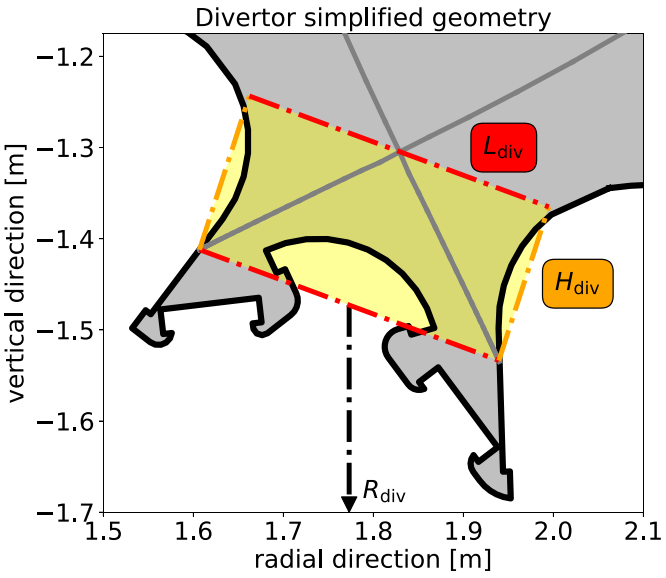

Figure 1. View in the poloidal plane of the DTT's diverted single null plasma of Moscheni *et al* [76, 77]: wall in black; interior of the chamber in light grey; separatrix in dark grey; simplistic rectangular representation of the divertor in yellow; segment connecting inner, left, and outer, right, strike points in dash-dotted red (of length L_{div}, with the radial location of its mid-point being R_{div}); H_{div} is the distance of the X-point from it (orange).

- ☐ The power crossing the separatrix P_{sep};
- ☐ A generalised power fall-off length for tokamaks which combines Eich's regression #14 [78], i.e. $\lambda_q^{E}[\text{mm}] = 0.63 \times (B_{pol}[\text{T}])^{-1.19}$, with the Scarabosio's correction factor f^{S} [79–82], such that: $f^{S} = 1$ for H-modes and $f^{S} = 2$ for L-modes; not enough data are presently available to include the turbulence-driven broadening of [83] and/or Goldston's heuristic model [84], which are worth considering in the future nonetheless;
- ☐ The Greenwald density limit $n^{G}[\text{m}^{-3}] = 10^{20} \times I_p[\text{MA}]/[\pi\,(a[\text{m}])^2]$ [85] and, additionally, the H–L density limit $\sim 0.45 \times n^{G}$ from Eich *et al* [86] (HDL), valid for H-mode tokamak plasmas [87]; stellarators instead abide to the Sudo density limit n^{Su} [88];
- ☐ The separatrix electron density at the outer mid-plane n_{sep};
- ☐ The opaqueness $n_{sep} \times a$, from a re-adaptation of the original definition from pedestal studies [89–91].

2.2.3. Engineering actuators. If not specified otherwise, the puffing rates of deuterium Γ_D and seeded impurities Γ_Z are converted to their electron-equivalent $[\text{el} \times \text{s}^{-1}]$ via the species atomic number [14].

Only puffing-dominated cases are included in the database, where any core fuelling rate is negligible compared to Γ_D [92], and other net particle sources/sinks (e.g. wall outgassing/retention [93]) can also be reasonably assumed as such.

Table 1 illustrates the vast range of cases included, with the actual rates spanning almost 5 orders of magnitude, and the ratio Γ_D/Γ_Z changing from impurity-dominated ($\ll 1$) to fuel-dominated ($\gg 1$) scenarios.

2.2.4. Detachment characterisation. The data are extracted at one or more time instants during the detached phase of the outer target—the only target considered for reasons of data availability and, with the exception of spherical tokamaks [10], for usually being the most loaded [75] and the last one to detach [12].

Among the methods proposed [40, 94–97], the degree of detachment (DOD) is *qualitatively* referred to in the present work. Its original definition reads:

$$\text{DOD} = \frac{\Gamma_{D^+}^{2PM}}{\Gamma_{D^+}^{meas}} \tag{3}$$

where $\Gamma_{D^+}^{2PM} \sim n_{sep}^2$ is the integrated main ion flux at the divertor target as estimated from the 2-point model (2PM) [7]—or from its readaptation to stellarators [98], and $\Gamma_{D^+}^{meas}$ is the same flux actually measured (from experiments or simulations).

Because only detached cases are here considered, DOD $=$ 1 specifically identifies the detachment onset during a density/puffing ramp, i.e. either (i) the appearance of ion-flux roll-over [14, 95, 99] or, if unavailable, (ii) the electron temperature dropping to $\sim$5 eV around the outer strike point [25, 61, 69, 100, 101], or (iii) when explicitly indicated by the author. Instances more deeply detached than the onset are labelled by DOD$>$1.

Main features of the DOD$>$ 1 and DOD $=$ 1 sub-sets are separately collated in table 1, and further details are given below.

2.3. Statistics

The errors and limited data availability of a real-world database dictate the statistical methods required for an appropriate assessment—herein devised around the Occam's Razor heuristic [102].

2.3.1. Statistical distinguishability. Throughout the paper, the permutation test of difference in linear intercepts (with significance level of 5%) [103] is used to assess whether two sub-sets are statistically distinguishable—i.e. if there is supporting evidence in affirming that the two sub-sets differ with respect to a variable (or a collection of).

2.3.2. Physics-informed step-wise fitting method. The suitability of the data fitting is indicatively quantified on the basis of R^2, though recognising that the model validation is the true judgement metric (section 2.3.5).

Generalising the recommendation of Zohm *et al* [8] that fitting functions should be 'motivated by experimental observations or physical arguments', but acknowledging the concerning finding of Body *et al* [39] that 'the apparent power law sensitively depends on the exact points used to build a scaling',

a step-wise approach is herein adopted: (i) physics-centred correlations are first sought in ascending complexity; (ii) empirical calibration factors are added where improving validation; only in case (i) and (ii) were to fail, (iii) linear regression is resorted upon—preferring N fitting parameters over $(N+1)$ to reduce the risk of over-fitting, modulo a marginal loss in R^2. And crucially, minimising the number of parameters maximises the data availability. Finally, (iv) well-established physical arguments are implemented in the laws discovered, to provide either upper bounds or meaningful simplifications.

2.3.3. Error sources. Disparate sources of error affect the data. From the perspective of the user, an unbiased, graphic data extraction error (digitisation error) of up to $\sim$15% can be assumed affecting any datum pinpointed in a plot and not explicitly quoted in the text of the parent paper. Also unbiased, though not quantifiable, is any transcription/typographical error.

Data-points from simulations feature convergence/discretisation errors—precisely defined [104, 105], but seldom assessed. Conversely, model errors are subtle, can change the detachment onset [106] and can be noticeable even for a fixed scenario of a single machine [28]—but are constantly being researched with studies across [21, 76, 77] and within [107–109] simulation codes. The occasional struggle experienced in jointly replicating experimental data and puffing rates (or pressures) in present-day machines [110–113] further testifies to the uncertainty of the puffing rates.

Regarding experimental data, Henderson *et al* [114] raise another issue specific to puffing: 'Requested flow rates [...] do not necessarily represent exactly the true injected flow rates'. Furthermore, diagnostic limitations affect the accuracy of experimental data—from magnetic reconstruction errors comparable to characteristic plasma length scales upstream (for n_{sep}) [42, 73, 100, 115, 116], to Langmuir probes struggling in recombining detached plasmas downstream (for DOD $= 1$ identification) [53, 117, 118]. Unaccounted intrinsic impurities (e.g. carbon) further contribute to data scatter.

To conclude with a positive note—the inherent uncertainty renders low-level operational differences indistinguishable, thereby allowing for the identification of robust scaling laws applicable across the entire database.

2.3.4. Non-comparability. Common to both experimental and numerical data, an overarching confounding factor arises from the 'partiality' of detachment (section 2.2.4). DOD varies continuously within $[1;+\infty)$, but quantifications of its value in the literature are practically inexistent. And instances at different, unquantified DOD lack direct comparability—points at different DOD would never precisely follow a scaling law which does not feature DOD among its variables.

2.3.5. Validation and definition of success. The sub-set of data at the detachment onset offers a solution to the above-mentioned complexities. Because DOD $= 1$ by definition, such cases are directly comparable and, in principle, could be described by a scaling law agnostic of DOD. However, as for table 1, only a maximum of 45 DOD $= 1$ data-points are available (reducing down to 16 in certain applications). *Per se*, this is statistically unsuitable.

On the other hand, in the sense of section 2.3.1, it is anticipated that there is no evidence throughout this study that the sub-set of DOD $= 1$ data lies systematically below its DOD>1 counterpart, (figure 2, bottom left), i.e. higher puffing does not necessarily imply higher DOD.

A first clear example is provided by De Gianni *et al* [119]: even within the same device and for otherwise same input parameters, (i) $\Gamma_{\mathrm{D}} = 3.6\times10^{22}$ el $\times$ s^{-1} leads to DOD $= 1$ while (ii) the combination $\Gamma_{\mathrm{D}} = 2.4\times10^{22}$ el $\times$ s^{-1} and $\Gamma_{\mathrm{Z}} = 0.3\times10^{22}$ el $\times$ s^{-1} results in DOD>1 despite the lower fuel, and total, puffing. The same is found by Lore *et al* [28], with $\Gamma_{\mathrm{D}} = 1.95\times10^{23}$ el $\times$ s^{-1} and $\Gamma_{\mathrm{Z}} = 0.40\times10^{23}$ el $\times$ s^{-1} resulting in a more deeply detached state than $\Gamma_{\mathrm{D}} = 5.85\times10^{23}$ el $\times$ s^{-1} and $\Gamma_{\mathrm{Z}} = 0.06\times10^{23}$ el $\times$ s^{-1}. Similar behaviours are even more likely to occur across scenarios and/or devices, when accounting for additional variables, non-linearities (e.g. see n_{sep} in figure 4(b) of [28]) and due to errors (section 2.3.3)—each alone potentially turning the bottom-left situation in figure 2 to the bottom-right one.

Therefore, DOD>1 points are found to provide a source of *unbiased* scatter around DOD $= 1$ (figure 2, bottom right), presumably further aided by the scarcity of deeply detached scenarios (DOD$\gg1$). This allows for devising a robust strategy as follows.

Database splitting:

- ☐ Training set: DOD>1 data are exclusively used to infer scaling laws;
- ☐ Validation set: the scaling laws are validated against the unseen, comparable DOD $= 1$ data.

The outcome of our study is therefore only applicable to DOD $= 1$ data, and scored[7] based on criteria that reflect the impact of the sources of error of section 2.3.3.

Definition of success[8]:

- ■ for agreement within a factor 1.5;
- ■ for agreement within a factor 3.0;
- ■ for agreement within a factor 6.0;
- ■ for anything worse.

The average factor of agreement is quantified via the arithmetic and geometric averages[9]. The latter is a better representation in cases where a single instance of poor agreement significantly distorts the arithmetic average.

Finally, the above-mentioned examples from De Gianni *et al* [119] and Lore *et al* [28] also suggest that results from the present study only inform around a sufficient, though not

[7] The colour scoring is inspired by the finely-crafted table 2 of Oliveira and Body *et al* [120].

[8] For reference, a 2D edge plasma simulation would likely require $\lesssim 10\%$ of the total computational time to reconverge after adjusting a puffing rate by a factor 1.5.

[9] I.e. $\sum_{i=1}^{n} X_i/n$ and $(\prod_{i=1}^{n} X_i)^{1/n}$, respectively.

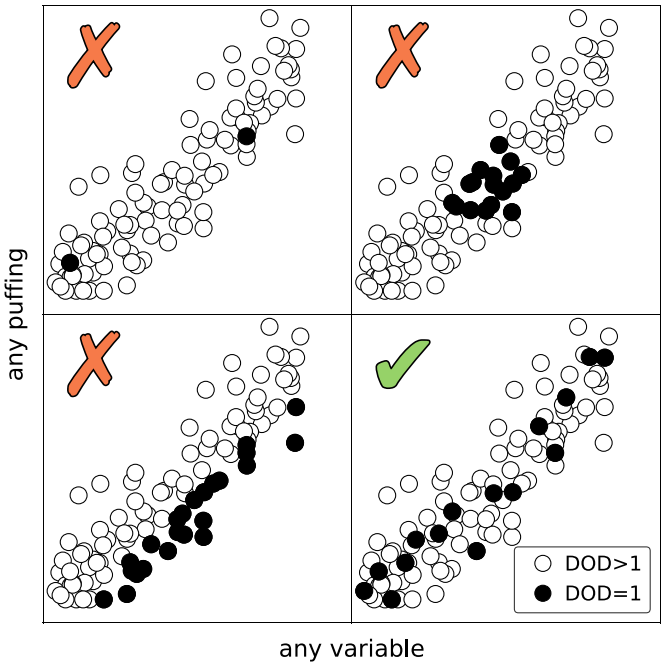

Figure 2. Illustrative instances with dummy data where the strategy devised in section 2.3.5 does (green tick) and does not (red crosses) work. Top left: the number of DOD = 1 points (black dots) is too small for validation. Top right: DOD = 1 points are too clustered within the DOD>1 points in white. Bottom left: DOD = 1 points are systematically below the rest. Bottom right: actual case, where DOD = 1 points are well distributed (see text for details).

necessary, condition for detachment access. Different fuel-impurity combinations leading to the same DOD might be possible.

3. Results

Plots in the following do contain both training (DOD>1) and validation (DOD = 1) data-points for the sake of completeness. Data belonging to each family are highlighted in dedicated figure insets, for a visual demonstration of their resemblance to figure 2 (bottom right). According to section 2.3.2, different scaling laws are built with incremental complexity and presented with their accompanying R^2.

3.1. Scaling laws for the fuel puffing rate

3.1.1. Dominant role of geometry: correlation with volume. Figure 3(*a*) illustrates the strong linear correlation between the fuel puffing rate Γ_D and the divertor volume V_{div}. Mathematically ($R^2 = 62\%$):

$$\Gamma_D^{VOL}\left[\text{el}\times\text{s}^{-1}\right] = 4.34\times10^{21}\times V_{div}\left[\text{m}^3\right]\ . \qquad (4)$$

This relationship highlights the fundamental role geometry plays, in fact encompassing most of the machine-specific details and operational variations across conventional, spherical and high-field tokamaks, stellarators and even linear plasma devices (section 2.1). On the one hand, only retaining the conventional tokamaks—which dominate the dataset—does not produce a measurable variation (section 2.3.1), as the cumulative number of entries from the other devices is comparatively small. For the same reason, it is not currently possible to derive statistically significant laws specific to the remaining four machine types.

Of note—despite the renowned operational differences [121], no statistically significant discrepancy is found between carbon machines (e.g. DIII-D [122]) compared to their metallic counterparts (e.g. the tungsten-walled AUG [123]). The absence of a difference in this respect was similarly found by Eich *et al* [78] concerning the power fall-off length.

The linear plasma devices DT-ALPHA ('DA' [124]) and TPD-Sheet IV ('TS' [125]) lying above the trend is ascribed to under-estimating the total volume (the volumes of the interconnections between chambers are unaccounted for). Among the remaining notable outliers in figure 3(*a*), both the family of metallic high-field tokamaks (i.e. Alcator C-Mod [90] and SPARC [50]), the carbon-walled NSTX [126, 127] and NSTX-U [69] are found to deviate from the average trend in the top-left area, MAST-U [128] in the bottom-right one. Distinctive feature of such devices is their exceptional separatrix electron density n_{sep}—and corresponding exceptional opaqueness.

3.1.2. Secondary physics dependency: correlation with opaqueness. Figure 3(*b*) evidences how including n_{sep} alongside geometry suffices in unifying the Γ_D behaviour—in an instance where an empirically-calibrated physics-based dependency outperforms purely-empirical linear regressions (section 2.3.2). In particular, the opaqueness $n_{sep}\times a$ appears ($R^2 = 67\%$):

$$\Gamma_D^{OPQ}\left[\text{el}\times\text{s}^{-1}\right] = 2.66\times10^3 \times\left[\left(n_{sep}\left[\text{m}^{-3}\right]\times a\,[\text{m}]\right)\times\left(\frac{S_{div}\left[\text{m}^2\right]}{V_{div}\left[\text{m}^3\right]}\right)^{-1.5}\right]^{1.05}\ . \qquad (5)$$

Geometry-wise, equation (5) relates compact divertors (high[10] S_{div}/V_{div}) with a reduced Γ_D, for a given opaqueness. No dependence on aspect ratio is found, as expected from [129]—where A varies from 1.4 to 2.8, but opaqueness and fuelling do not.

Physically, that n_{sep} matters across machines is natural. For instance, $n_{sep}\sim 8\times10^{19}$ m^{-3} in high-field tokamaks is a factor ~3 above that of H-mode plasmas in the other devices. Conversely, no such relationship of Γ_D with the line-average electron density n_{avg} holds. The puffed fuel is unable to penetrate the confined plasma deep enough for an effect on n_{avg} to surface [89–91, 100].

[10] For a fixed shape, e.g. a sphere of radius r, $S/V = 3/r$ and the ratio (and the compactness) increases as r drops.

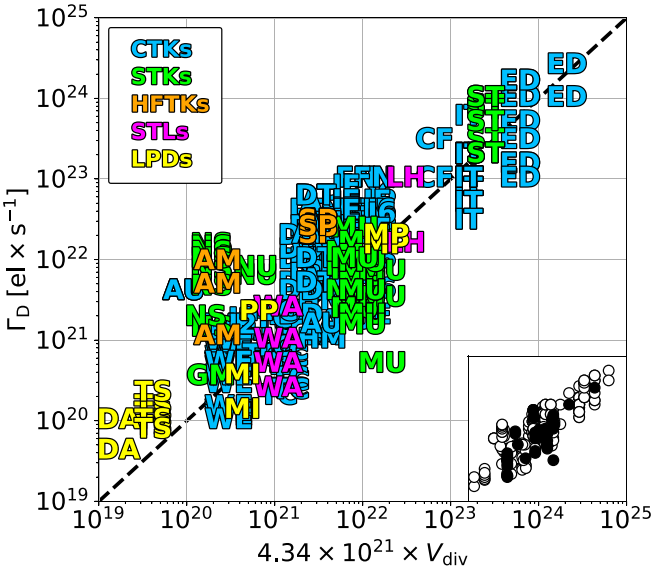

(a)

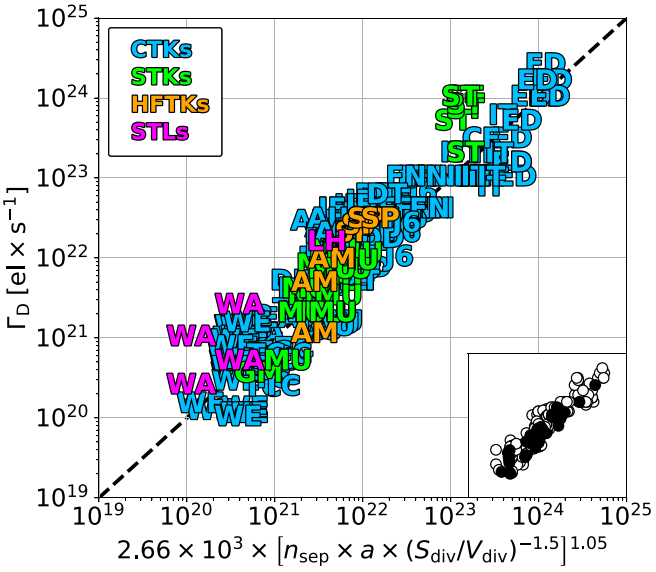

(b)

Figure 3. Results for the fuel puffing rate Γ_D from: (*a*) the geometry-based equation (4) (VOL), exclusively depending on the divertor volume V_{div}; (*b*) equation (5) (OPQ), where the opaqueness at the outer mid-plane separatrix $n_{sep} \times a$ appears alongside empirical calibration factors (exponents). Insets in the bottom right corners highlight points at DOD = 1 (black) and DOD>1 (white) within the main plot. Scaling laws are derived from DOD>1 points only (training set).

3.2. Scaling law for the impurity puffing rate

3.2.1. Generalities. As shown in figure 4(*a*) and in contrast to Γ_D, the impurity puffing rate Γ_Z is not correlated to the divertor volume V_{div}. This feature could be explained, in part, by the residence time in the edge plasma $\tau \sim L_{conn}/c_s$, where $L_{conn} \sim \pi a B_{tor}/B_{pol}$ is the connection length (outer mid-plane to target) and $c_s \sim T^{1/2}$ the plasma sound speed [7]. Whether $T = T_{sep}$ ($\sim R_0^{0.57}$ across the database) or $T \sim 5$ eV (in the detached zone) or a combination of the two is best suited to compute the sound speed, c_s mildly increases with machine size at best. Therefore, τ must increase because of the leading dependence on connection length ($L_{conn} \sim R_0^{0.64}$ in the database).

The counter-intuitive, and somewhat surprising, result is that impurity puffing rates can be similar in a machine the size of COMPASS [130] ($R_0 \sim 0.6$ m, $V_p \sim 1$ m^3 and $P_{sep} < 1$ MW) and in ITER [131] ($R_0 \sim 6$ m, $V_p \sim 900$ m^3 and $P_{sep} \sim 100$ MW). The average seeding rates in the database indeed read $\Gamma_Z \sim 2 \times 10^{21}$ el × s^{-1} and 3×10^{21} el × s^{-1} for the two machines, respectively.

3.2.2. Linear regression of non-linear function. Operationally, the impurity seeding Γ_Z is usually added on top of fuel puffing Γ_D, and is hence expected to be a function of the Γ_D level itself. Furthermore, the complexity of (i) the impurity transport [108, 132], (ii) the radiation efficiency [133–135] and (iii) the involved interplay between $\Gamma_D + \Gamma_Z$ and Γ_D/Γ_Z (figure 4(*b*) of [28]) hint at the presence of significant non-linearities—in the words of Body *et al* [39]: 'the impurity concentration required for detachment does not follow a simple power law'. Last, (iv) it is noted that reactor-relevant puffing ratios $\Gamma_D/\Gamma_Z \gg 1$ are achieved in bigger machines by means of high total puffing $\Gamma_D + \Gamma_Z \gg 1$, and vice versa for smaller ones.

Therefore, a Boolean-'AND' non-linear function able to account for all of the above is considered:

$$\gamma_{DZ} = (\Gamma_D + \Gamma_Z) \times (\Gamma_D/\Gamma_Z) \ , \tag{6}$$

which necessitates of the reactor-relevant condition $\Gamma_Z > 0$. This allows for establishing the satisfactory linear regression pictured in figure 4(*b*) ($R^2 = 48\%$):

$$\begin{aligned}\gamma_{DZ}\left[\text{el} \times \text{s}^{-1}\right] = 1.40 \times 10^{-11} &\times \left(L_{div}\left[\text{m}\right]\right)^{-0.05} \\ &\times \left(H_{div}\left[\text{m}\right]\right)^{2.5} \times \left(R_{div}\left[\text{m}\right]\right)^{1.0} \\ &\times \left(n_{sep}\left[\text{m}^{-3}\right]\right)^{1.8} \ .\end{aligned} \tag{7}$$

Knowing the value of γ_{DZ}, the impurity puffing rate is then computed by solving equation (6) for Γ_Z:

$$\Gamma_Z\left[\text{el} \times \text{s}^{-1}\right] = \frac{\left(\Gamma_D^{OPQ}\left[\text{el} \times \text{s}^{-1}\right]\right)^2}{\gamma_{DZ}\left[\text{el} \times \text{s}^{-1}\right] - \Gamma_D^{OPQ}\left[\text{el} \times \text{s}^{-1}\right]} \ , \tag{8}$$

where the fuel puffing rate is that of equation (5). In contrast to the fuelling rate, but coherently with the aforementioned non-linearities, a non-trivial dependence of Γ_Z on n_{sep} is found—both γ_{DZ} and Γ_D in equation (8) depend on it.

Finally, differences in impurity species are also embedded in γ_{DZ}—operation in smaller devices favours low-Z impurities, and viceversa.

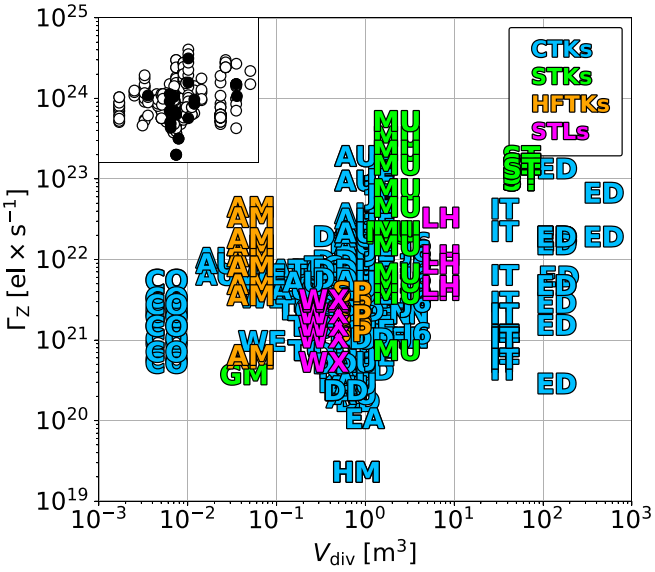

(a)

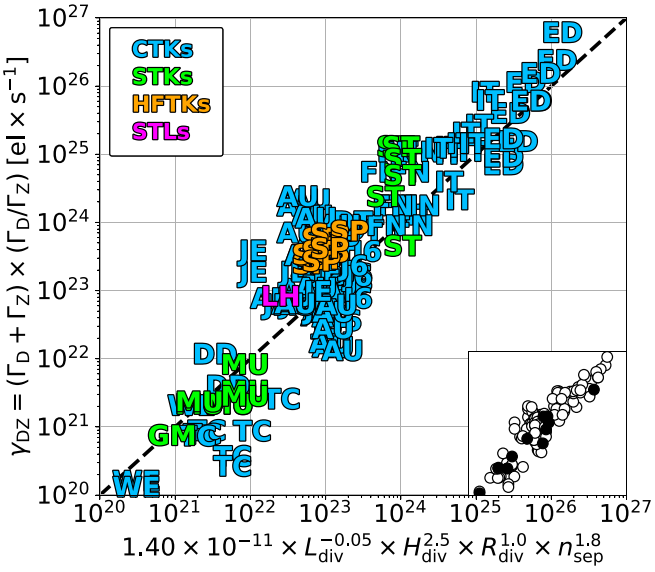

(b)

Figure 4. (*a*) Lack of correlation of the impurity puffing rate Γ_Z with the divertor volume V_{div}. (*b*) Result of equation (7) for the non-linear function $\gamma_{DZ} = (\Gamma_D + \Gamma_Z) \times (\Gamma_D/\Gamma_Z)$.

3.3. Simplified scaling laws

The presence of n_{sep} in equation (5) for Γ_D and in equation (8) for Γ_Z introduces a layer of complexity [42, 78] that simplified physics models [10, 39–45], AI-based ones [37, 38] or other extrapolations [3, 136] can synergistically address. Indeed, the value of n_{sep} is usually quantified before puffing rates are [3, 137].

Nonetheless, physics-based approximations agnostic of n_{sep} are sought in the light of section 2.3.2.

3.3.1. Tokamaks: density limits and power fall-off length.

An approximation for the tokamak's fuelling rate is found by rearranging equation (5) by means of: (i) equation (2); (ii) loosely capping n_{sep} via HDL ($\lesssim 0.45 \times n^G$, section 2.2.2); (iii) the generalised power fall-off length (section 2.2.2); (iv) the definition of poloidal magnetic field $B_{pol}[T] = \mu_0 I_p[A]/(2\pi a[m])$. Ultimately, the HDL loose upper bound reads:

$$\Gamma_D^{HDL}\left[\text{el} \times \text{s}^{-1}\right] \sim 0.45^{1.05} \times \Gamma_D^{GES}\left[\text{el} \times \text{s}^{-1}\right] , \qquad (9)$$

where Γ_D^{GES} represents the Greenwald–Eich–Scarabosio (GES) strict upper bound ($n_{sep} < n^G$):

$$\Gamma_D^{GES}\left[\text{el} \times \text{s}^{-1}\right] \sim 1.0 \times 10^{23} \times (a\,[\text{m}])^{1.58} \times \left(\lambda_q^E\,[\text{mm}] \times f^S\,[-]\right)^{-0.89} . \qquad (10)$$

It is worth noting that the HDL loose upper bound requires $f^S = 1$, and that the GES strict upper bound only applies for DOD = 1, at least in its present form.

For Γ_Z, the non-linearities involved in equation (8) mean that well-defined, general upper bounds can not be found. Therefore, n_{sep} is directly proxied with the Greenwald density limit[11], as accomplished in [78]. Leveraging the fact that $28 \times (\lambda_q^E[\text{mm}] \times f^S[-])^{-0.62} \gg 1$, equation (8) becomes:

$$\Gamma_Z^{GES}\left[\text{el} \times \text{s}^{-1}\right] \sim 3.6 \times 10^{21} \times (a\,[\text{m}])^{1.51} \times \left(\lambda_q^E\,[\text{mm}] \times f^S\,[-]\right)^{-0.27} , \qquad (11)$$

applicable for both L- and H-modes.

The negative correlations to λ_q^E further hint at the role of neutral penetration. Indeed, a figure of merit for neutral fuelling by means of puffing is the neutral mean free path (mfp) normalised to the minor radius—i.e. $\text{mfp}/a \sim B_{pol}^{-1}$, close to the density limit [138]. Therefore, it holds that $\text{mfp}/a \sim \lambda_q^E$, and the mean free path is approximately proportional to the power fall-off length.

3.3.2. Stellarators: Sudo density limit.

Algebra equivalent to that of section 3.3.1 with the Sudo density limit [88] leads to the stellarator strict upper bound ($n_{sep} < n^{Su}$):

$$\Gamma_D^{Su}\left[\text{el} \times \text{s}^{-1}\right] \sim 2.2 \times 10^{22} \times (a\,[\text{m}])^{1.58} \times \left(\frac{P_{in}\,[\text{MW}] \times B_{tor}\,[\text{T}]}{R_0\,[\text{m}]}\right)^{0.53} , \qquad (12)$$

and the proxy ($n_{sep} \sim n^{Su}$):

$$\Gamma_Z^{Su}\left[\text{el} \times \text{s}^{-1}\right] \sim 2.4 \times 10^{21} \times (a\,[\text{m}])^{1.51} \times \left(\frac{P_{in}\,[\text{MW}] \times B_{tor}\,[\text{T}]}{R_0\,[\text{m}]}\right)^{0.16} , \qquad (13)$$

[11] Proxying via HDL would give a mere ∼20% variation—negligible compared to the other intrinsic uncertainties and approximations involved in deriving the simplified laws.

where P_{in} represents the absorbed input power, B_{tor} the toroidal magnetic field on axis. The reader is referred to section 2.4.2 of Greenwald [138] for uncertainties in stellarator density limits.

3.4. Validation

The validation of the different scaling laws computed from the DOD>1 data-points is performed against the unseen DOD = 1 sub-set. The results are summarised in table 2 according to the indications of section 2.3.5, with the asterisked entries being from experimental data and the superscripts specifying the L/H confinement mode (if available).

No systematic bias is detected among the predicted values, as expected from section 2.3.5 (figure 2), and the validation is satisfactory as a whole. Γ_D and Γ_Z predictions are found to be accurate within a factor ∼2 on average (table 2, last row, with the geometric average within round brackets).

Under-represented machine types are the linear plasma devices and the stellarators. For the former, only Magnum-PSI (#31) suggests a potential for good agreement—but via the geometry-based equation (4) (VOL), the only one valid for linear plasma devices. No stellarator case at DOD = 1 is available, and the applicability of the scaling laws is therefore questionable in their respect. However, it is noted that stellarators never represented an anomaly compared to the other devices within this study.

3.4.1. Validation of scaling laws for fuel puffing rates.

Equation (5) (OPQ) outperforms the geometry-based equation (4) (VOL) by virtue of the opaqueness dependence. This is not ubiquitous, but clearly present for the high-density tokamaks DTT (#9), NSTX-U (#32-33) and SPARC (#34), where Γ_D^{VOL} underestimates the true value by an order of magnitude. Equation (4) (VOL) tends to overestimate Γ_D in MAST-U cases (#21-30)—and equation (5) (OPQ) addresses that shortcoming.

The looseness of the HDL upper bound of equation (9) surfaces in 5/15 instances, where Γ_D^{HDL} is overcome by the actual Γ_D. Although the limited data availability hinders further insight in such cases, estimates are presumably affected by, at least: (i) the very HDL definition in section 2.2.2 which involves the 0.45 factor (∼0.4–0.5 in the original work [86]); (ii) the approximations adopted in the computation of Γ_D^{HDL} (section 3.3.1); (iii) the applicability of the HDL only to cases featuring a ballooning parameter ∼2.0–2.5 [86], which is not herein quantifiable. That (i) matters is suggested by the JT-60SA entries (#17 to #20), for which n_{sep}/n^G grows from 0.20 to 0.34, hence approaching the ∼0.45 mark and achieving increasingly better accuracy accordingly. On average, Γ_D^{HDL} is found to be accurate within a factor 2.3 for H-modes. Crucially, it provides reliable estimates when n_{sep} is not available and equation (5) (OPQ) can not be used (e.g. #23-24-28)—i.e. the very reason why the HDL equation (9) was devised in the first place.

Finally, the GES strict upper bound (equation (10), grey in table 2) sets a limit overcome neither by the actual Γ_D nor by equation (5) (OPQ) it is derived from.

3.4.2. Validation of scaling laws for impurity puffing rates.

The validation of impurity puffing rates is successful for conventional tokamaks despite the reduced data availability. Presumably due to tapering of the non-linearities and bearing intrinsic physical meaning (section 4.8), the GES proxy in equation (11) (GES) tends to even outperform its original version (equation (8), via γ_{DZ})—equally in H- and L-modes.

Instead, impurity-seeded spherical tokamaks are under-represented. Mixed success is achieved in MAST-U cases, particularly at the extrema of DOD = 1 with high seeding (#21, $\Gamma_Z = 1.7 \times 10^{23}$ el × s^{-1} with conventional divertor) and low seeding (#30, $\Gamma_Z = 7.0 \times 10^{20}$ el × s^{-1} with Super-X divertor). The fact that spherical tokamaks feature higher impurity puffing rates (figure 4(*a*)) might play a role, but attempts at including an aspect ratio dependence in equation (7) which validate well proved unsuccessful. However, the two instances of agreement (#22-30) give confidence that spherical tokamaks could be described by simple scaling laws too.

4. Discussion

4.1. Interpretation and applicability of the scaling laws

Generally speaking, caution is required when interpreting any scaling laws, as correlation does not necessarily imply causation. In the present case, additional care is warranted because the laws are validated specifically for plasmas at detachment onset (DOD = 1).

For instance, a conceptual experiment in which P_{sep} is increased would, in practice, cause the DOD = 1 plasma to reattach (DOD<1). The comparable DOD = 1 condition could only be restored by enhancing Γ_D and/or Γ_Z, which would in turn affect n_{sep} and other correlated quantities [28]. As a consequence, disentangling the influence of individual, potentially co-varying parameters remains challenging.

This also highlights that our scaling laws describe transitions between DOD = 1 states, rather than time evolution within a given discharge.

In this sense, the present study should be viewed as a *macroscopic* analysis—capturing trends *across* devices, but not necessarily *within* any single machine. The dominant dependencies in this regime are geometric—equation (4) being the leading example. As such, the scaling laws inform comparisons/extrapolations between machines, but do not necessarily describe the time-dependent response of a specific device unless, perhaps, its geometry changes significantly (see, e.g. the CRD in section 4.4.2).

Figure 5 pictorially illustrates this concept. Each coloured segment represents the behaviour of an individual machine, following its own local trend—simplistically

Table 2. Validation of the scaling laws computed with DOD>1 data against the unseen DOD = 1 data (units $[\mathrm{el}\times\mathrm{s}^{-1}]$, machine IDs from appendix). Colour scoring (section 2.3.5): for agreement within a factor 1.5; within 3.0; within 6.0; anything worse; for the strict upper bound (equation (10)). White cells are either the actual puff rates, or predictions lacking the actual rate for comparison, or not available (–). Superscripts identify experimental data (*) and confinement mode (L)/(H). Last row: factor of agreement as arithmetic (geometric) average.

#	ID [reference]	Γ_D	Equation (4) VOL	Equation (5) OPQ	Equation (9) HDL	Equation (10) GES	Γ_Z	Equation (8) via γ_{DZ}	Equation (11) GES
1	AU$^{(L)}$* [139]	7.0×10^{21}	3.4×10^{21}	4.0×10^{21}	—	8.1×10^{21}	9.8×10^{20}	4.6×10^{20}	8.2×10^{20}
2	AU$^{(L)}$* [95]	1.2×10^{21}	3.4×10^{21}	3.4×10^{21}	—	1.0×10^{22}	—	4.4×10^{20}	8.8×10^{20}
3	AU$^{(L)}$ [140]	4.0×10^{21}	3.4×10^{21}	3.3×10^{21}	—	1.0×10^{22}	—	4.4×10^{20}	8.8×10^{20}
4	AU$^{(L)}$ [141]	5.8×10^{21}	3.4×10^{21}	5.3×10^{21}	—	1.0×10^{22}	—	4.8×10^{20}	8.8×10^{20}
5	CF$^{(H)}$ [142]	1.0×10^{23}	6.6×10^{22}	1.6×10^{23}	1.7×10^{23}	4.0×10^{23}	—	6.5×10^{21}	8.9×10^{21}
6	DD$^{(H)}$* [122]	—	2.0×10^{21}	3.0×10^{21}	1.3×10^{22}	2.9×10^{22}	1.4×10^{21}	2.2×10^{21}	1.6×10^{21}
7	DD$^{(H)}$* [122]	—	2.0×10^{21}	2.7×10^{21}	1.3×10^{22}	2.9×10^{22}	3.5×10^{21}	2.2×10^{21}	1.6×10^{21}
8	DD$^{(H)}$* [122]	—	2.0×10^{21}	2.4×10^{21}	1.3×10^{22}	2.9×10^{22}	7.0×10^{21}	2.3×10^{21}	1.6×10^{21}
9	DT$^{(H)}$ [26]	6.0×10^{22}	2.9×10^{21}	2.3×10^{22}	6.0×10^{22}	1.4×10^{23}	5.5×10^{21}	1.8×10^{21}	2.8×10^{21}
10	ED$^{(H)}$ [143]	—	6.5×10^{23}	4.5×10^{23}	4.1×10^{23}	9.4×10^{23}	5.8×10^{21}	1.7×10^{22}	2.1×10^{22}
11	ED$^{(H)}$ [144]	5.0×10^{23}	6.1×10^{23}	6.4×10^{23}	4.8×10^{23}	1.1×10^{24}	1.8×10^{22}	1.2×10^{22}	2.2×10^{22}
12	HA$^{(L)}$* [47]	—	2.0×10^{21}	7.6×10^{20}	—	1.2×10^{21}	4.8×10^{20}	1.6×10^{20}	3.7×10^{20}
13	JE$^{(L)}$ [145]	8.0×10^{21}	4.7×10^{21}	6.0×10^{21}	—	4.4×10^{22}	—	2.7×10^{21}	3.5×10^{21}
14	JE$^{(L)}$ [145]	9.0×10^{21}	4.7×10^{21}	5.6×10^{21}	—	4.4×10^{22}	—	2.7×10^{21}	3.5×10^{21}
15	JE$^{(L)}$ [145]	5.0×10^{21}	8.8×10^{21}	8.3×10^{21}	—	4.4×10^{22}	—	2.6×10^{21}	3.5×10^{21}
16	JE$^{(L)}$* [72]	2.3×10^{22}	1.5×10^{22}	1.5×10^{22}	—	3.9×10^{22}	—	1.4×10^{21}	3.4×10^{21}
17	J6$^{(H)}$ [25]	1.0×10^{22}	1.6×10^{22}	2.6×10^{22}	7.9×10^{22}	1.8×10^{23}	4.2×10^{21}	4.0×10^{21}	5.1×10^{21}
18	J6$^{(H)}$ [25]	2.0×10^{22}	1.6×10^{22}	3.1×10^{22}	7.9×10^{22}	1.8×10^{23}	2.8×10^{21}	4.1×10^{21}	5.1×10^{21}
19	J6$^{(H)}$ [25]	3.0×10^{22}	1.6×10^{22}	3.7×10^{22}	7.9×10^{22}	1.8×10^{23}	2.8×10^{21}	4.3×10^{21}	5.1×10^{21}
20	J6$^{(H)}$ [119]	3.6×10^{22}	1.6×10^{22}	4.5×10^{22}	7.9×10^{22}	1.8×10^{23}	—	4.4×10^{21}	5.1×10^{21}
21	MU$^{(H)}$ [61]	2.0×10^{21}	9.8×10^{21}	3.5×10^{21}	—	—	2.1×10^{23}	6.5×10^{21}	—
22	MU$^{(H)}$ [61]	2.0×10^{21}	9.8×10^{21}	2.0×10^{21}	—	—	2.1×10^{22}	4.8×10^{22}	—
23	MU$^{(H)}$* [114]	7.2×10^{21}	8.1×10^{21}	—	6.4×10^{21}	1.5×10^{22}	—	—	1.1×10^{21}
24	MU$^{(H)}$* [114]	1.0×10^{22}	8.1×10^{21}	—	6.4×10^{21}	1.5×10^{22}	—	—	1.1×10^{21}
25	MU$^{(L)}$* [128]	4.0×10^{21}	7.1×10^{21}	2.2×10^{21}	—	6.0×10^{21}	—	3.6×10^{21}	7.5×10^{20}
26	MU$^{(L)}$* [128]	5.0×10^{20}	1.7×10^{22}	1.4×10^{21}	—	6.0×10^{21}	—	3.3×10^{22}	7.5×10^{20}
27	MU$^{(H)}$* [97]	1.5×10^{21}	9.8×10^{21}	—	5.2×10^{21}	1.2×10^{22}	—	—	9.3×10^{20}
28	MU$^{(H)}$* [97]	6.0×10^{21}	9.8×10^{21}	—	3.5×10^{21}	8.2×10^{21}	—	—	8.3×10^{20}
29	MU$^{(H)}$ [101]	3.2×10^{21}	9.8×10^{21}	5.3×10^{21}	2.4×10^{21}	5.6×10^{21}	—	4.9×10^{21}	7.3×10^{20}
30	MU$^{(H)}$ [101]	2.0×10^{21}	9.8×10^{21}	4.5×10^{21}	2.4×10^{21}	5.6×10^{21}	7.0×10^{20}	5.3×10^{21}	7.3×10^{20}
31	MP* [52]	1.5×10^{22}	1.8×10^{22}	—	—	—	—	—	—
32	NU [69]	7.8×10^{21}	6.0×10^{20}	4.4×10^{21}	—	4.3×10^{22}	—	3.6×10^{21}	1.5×10^{21}
33	NU [69]	6.2×10^{21}	6.0×10^{20}	4.4×10^{21}	—	4.3×10^{22}	—	3.6×10^{21}	1.5×10^{21}
34	SP$^{(H)}$ [50]	3.0×10^{22}	3.1×10^{21}	1.6×10^{22}	5.3×10^{22}	1.2×10^{23}	1.4×10^{21}	1.3×10^{21}	2.0×10^{21}
35	TC$^{(L)}$* [146]	2.2×10^{21}	7.5×10^{20}	1.6×10^{21}	—	2.3×10^{21}	—	4.8×10^{20}	2.7×10^{20}
36	TC$^{(H)}$ [147]	6.0×10^{20}	1.5×10^{21}	1.6×10^{21}	1.1×10^{21}	2.6×10^{21}	—	3.2×10^{20}	2.8×10^{20}
37	WE* [148]	1.2×10^{20}	3.0×10^{20}	1.8×10^{20}	—	1.9×10^{22}	6.1×10^{21}	2.6×10^{20}	1.1×10^{21}
38	WE$^{(L)}$ [149]	1.0×10^{20}	3.0×10^{20}	3.8×10^{20}	—	4.4×10^{21}	—	1.2×10^{20}	5.4×10^{20}
39	WE$^{(L)}$ [149]	1.1×10^{20}	3.0×10^{20}	3.8×10^{20}	—	4.4×10^{21}	—	1.2×10^{20}	5.4×10^{20}
40	WE$^{(L)}$ [149]	2.8×10^{20}	3.0×10^{20}	3.6×10^{20}	—	4.4×10^{21}	—	1.2×10^{20}	5.4×10^{20}
41	WE$^{(L)}$ [149]	3.5×10^{20}	3.0×10^{20}	3.5×10^{20}	—	4.4×10^{21}	—	1.2×10^{20}	5.4×10^{20}
42	WE$^{(L)}$ [149]	4.9×10^{20}	3.0×10^{20}	3.4×10^{20}	—	4.4×10^{21}	—	1.2×10^{20}	5.4×10^{20}
43	WE$^{(L)}$ [149]	7.6×10^{20}	3.0×10^{20}	3.1×10^{20}	—	4.4×10^{21}	—	1.1×10^{20}	5.4×10^{20}
44	WE$^{(L)}$ [15]	9.7×10^{20}	3.0×10^{20}	3.7×10^{20}	—	5.3×10^{21}	—	1.2×10^{20}	5.8×10^{20}
45	WE$^{(L)}$ [147]	5.0×10^{20}	3.0×10^{20}	3.4×10^{20}	—	4.9×10^{21}	—	1.2×10^{20}	5.6×10^{20}
Avg. agreement:		—	4.2 (2.6)	1.9 (1.7)	2.3 (1.9)	—	—	5.6 (2.9)	2.1 (1.8)

assumed (log-)linear. The 'barycentric average' of these segments gives rise to the global, multi-machine scaling law. Specialising the present framework to the *microscopic* domain of a single device—where conditions vary continuously—forms part of our ongoing work, but is beyond the scope of the present one.

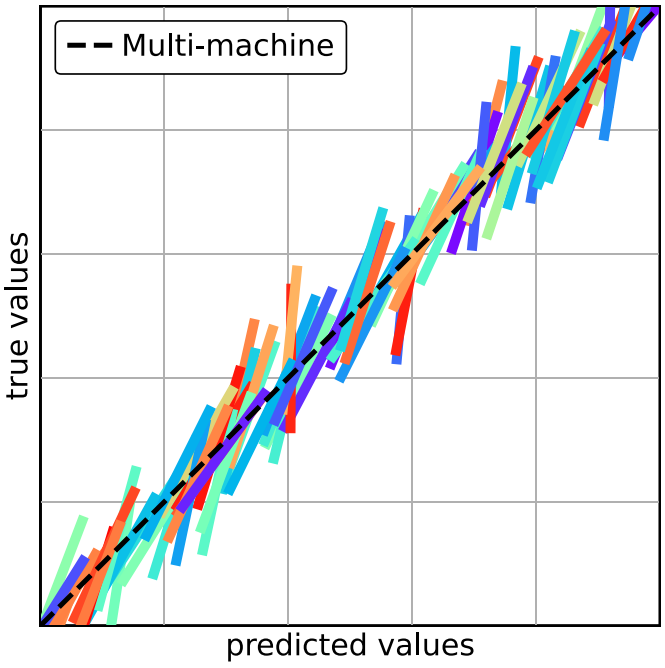

Figure 5. Pictorial interpretation with dummy data of a prototypical scaling law—that is a macroscopic model of the trends across devices (a 'barycentric average', dashed black line), but without necessarily being representative of each individual machine (coloured segments).

Finally, it should be emphasised that the absence of a given parameter in the empirical laws does not imply that it plays no physical role. Rather, it indicates that its effect is not discernible. This can result from a combination of uncertainties (section 2.3.3) and the aforementioned geometric dominance, which together tend to mask secondary dependencies.

Further adding to the above, an often overlooked source of conditioning may arise from the *operator bias*. Both experimental campaigns and edge plasma simulations naturally converge toward specific 'recipes' of control parameters that ensure effective operation or stable detached performance—such as maintaining a target n_{sep} or numerical convergence. As a result, the accessible parameter space is not uniformly sampled. Examples include the $\Gamma_{\mathrm{D}}/\Gamma_{\mathrm{Z}}$ ratios [28], tailored impurity mixtures [14], and effective pumping speeds (section 4.3).

'Empirical universality' partly reflects the community's convergence on similar operational strategies.

4.2. Position with respect to existing knowledge

Simplified analytical models have proven to be a reliable asset for 0.5D assessments of the edge plasma. The two fundamental approaches most commonly adopted [42, 150] are summarised by Body *et al* [39], and model inputs/outputs are exemplified by table 2 of Henderson *et al* [10].

Concerning the latter [10], we note that retrieving Γ_{D} and Γ_{Z} could be possible for tokamaks (units $[\mathrm{at}\times\mathrm{s}^{-1}]$). Indeed, two approximations for as many variables are available.

First, for single-null plasmas[12] equation (8) of [10] offers:

$$p_{\mathrm{div}} = \frac{\Gamma_{\mathrm{D}}+\Gamma_{\mathrm{Z}}+\Gamma_{\mathrm{core}}}{S_{\mathrm{eff}}} \times k_{\mathrm{B}} T_{\mathrm{pump}}\,, \tag{14}$$

where $S_{\mathrm{eff}}\,[\mathrm{m}^3\times\mathrm{s}^{-1}]$ is the effective pumping speed, $\Gamma_{\mathrm{core}}\,[\mathrm{at}\times\mathrm{s}^{-1}]$ is the core fuelling rate (known and usually such that[13] $\Gamma_{\mathrm{core}} \ll \Gamma_{\mathrm{D}}+\Gamma_{\mathrm{Z}}$ for DOD>1), and T_{pump} [K] is the pump duct temperature (commonly ∼300 K). These parameters are further commented in section 4.3.

Second, a relationship for the impurity concentration can be retrieved either (i) via equation (3) of [157] for an estimate of (an upper bound of) impurity concentration in the divertor:

$$c_{\mathrm{Z}} \lesssim \frac{\Gamma_{\mathrm{Z}}}{\Gamma_{\mathrm{D}}+\Gamma_{\mathrm{Z}}}\,, \tag{15}$$

or (ii) via one among equations (3–5) of [158] (for AUG) or equation (6) of [158] (for JET), with then $n_{\mathrm{sep}} \sim p_{\mathrm{div}}^{0.31}$ [10, 42].

While our 0D models utilise high-level, system-code-like parameters for input (see, e.g. table 3 of [159]), more sophisticated models like those of [10, 39] (0.5D) are designed to explore lower-level physics, and thus require more detailed inputs and underlying relationships. Given the proven usefulness of cross-comparisons between models of different fidelity [76, 77, 160] and dimensionality [101], one such exercise in the present context is believed to be valuable, but outside the scope of this work.

For instance, our work uses upper bounds for n_{sep} that are at times only loosely approached—a point of improvement for future studies. A cross-comparison with 0.5D models would involve testing their underlying scaling $n_{\mathrm{sep}} \sim p_{\mathrm{div}}^{0.31}$ [10, 42], whose exponent is currently uncertain—values ranging from $\leqslant 0.0$ and up to ∼0.55 have been found across different studies and seeding scenarios [7, 42, 44, 115, 161].

The discrepancies between equation (15) (i.e. equation (2) of [158]) and the trends in figure 4(*a*) of [28] are also noteworthy: $c_{\mathrm{Z}} \sim \Gamma_{\mathrm{Z}}$ vs. $c_{\mathrm{Z}} \sim \Gamma_{\mathrm{Z}}^{0.74}$ in the limit $\Gamma_{\mathrm{Z}} \ll \Gamma_{\mathrm{D}} = \mathrm{const}$; and $c_{\mathrm{Z}} \sim \mathrm{const}$ vs. $c_{\mathrm{Z}} \sim \Gamma_{\mathrm{Z}}^{-0.24}$ if $\Gamma_{\mathrm{D}}/\Gamma_{\mathrm{Z}} = \mathrm{const}$, respectively.

Because our equation (6) for γ_{DZ} scales similarly to equation (15), resolving these discrepancies (and those concerning $n_{\mathrm{sep}} \sim p_{\mathrm{div}}^{0.31}$) forms part of our current and forthcoming studies.

4.3. Puffing, pressure and pumping

Our results show that factor-2 accuracy can be obtained without explicit knowledge of S_{eff}, the effective pumping speed—a local quantity which would otherwise require a

[12] Hence without the factor 2 at the denominator.

[13] E.g. $\Gamma_{\mathrm{core}} \sim 10^{22}$ at $\times\,\mathrm{s}^{-1}$ corresponds to a mere 2%–10% of $\Gamma_{\mathrm{D}}+\Gamma_{\mathrm{Z}}$ in ITER for scenarios at high-enough DOD [28, 29]; $\Gamma_{\mathrm{core}} = 8\times10^{20}$ at $\times\,\mathrm{s}^{-1}$ is 4% of $\Gamma_{\mathrm{D}}+\Gamma_{\mathrm{Z}}$ in AUG [151–153]; $\Gamma_{\mathrm{core}} \sim 3\times10^{20}$ at $\times\,\mathrm{s}^{-1}$ (estimated from [154]) accounts for 6% in MAST-U [114]; $\Gamma_{\mathrm{core}} \sim 1\times10^{20}$ at $\times\,\mathrm{s}^{-1}$ (estimated from [155]) for $\lesssim$10% in TCV [156]. This also suggests that Γ_{core} itself might follow a specific pattern.

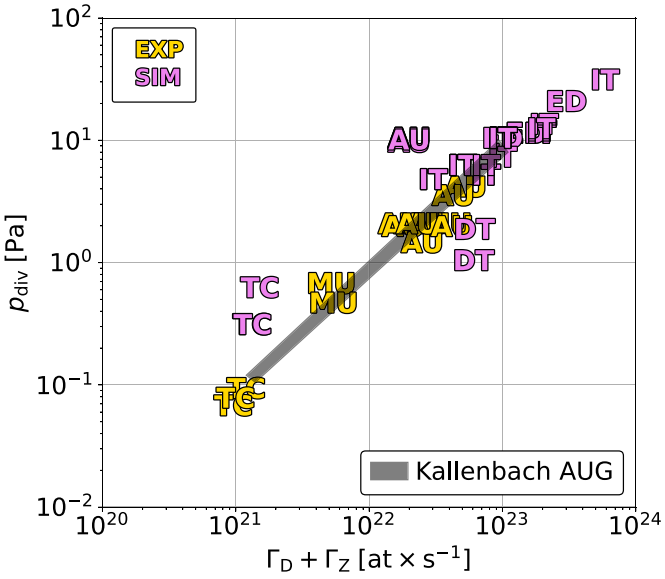

Figure 6. Divertor neural pressure p_{div} vs. total puffing rate for experimental (EXP) and simulated (SIM) cases in the present database. Overlaid in grey is the experimental result of Kallenbach *et al* [42] in AUG (figure 5 therein), including both attached and detached cases.

precise characterisation, depending on machine-specific hardware, its operating point, sub-divertor/duct geometry [162–166] and any wall contribution [93]. This suggests a degree of robustness in the proposed scaling laws.

At the same time, S_{eff} is recognised as a physically meaningful parameter whose role warrants further examination.

To explore this aspect, figure 6 plots p_{div} against the total puffing rate (in $[\text{at} \times \text{s}^{-1}]$) across our database, overlaid with the experimental result of Kallenbach *et al* [42] (figure 5 therein). The corresponding p_{div}-scaling reads ($R^2 = 47\%$):

$$p_{div}\,[\text{Pa}] = 6.5 \times 10^{-23} \times \left(\Gamma_D\left[\text{at} \times \text{s}^{-1}\right] + \Gamma_Z\left[\text{at} \times \text{s}^{-1}\right]\right), \quad (16)$$

and reproduces Kallenbach's best-fit almost exactly—despite the additional presence of attached cases in [42] (DOD<1).

The sample size remains however limited due to the inclusion of p_{div}, resulting in not insignificant scatter. *This strictly forbids any generalisation or claim of universality at this stage, as the observed pattern may in part be coincidental.*

Still, the trend of figure 6 suggests that the proportionality factor $\sim T_{pump}/S_{eff}$ in equation (14)—mainly depending on S_{eff}—is approximately constant within the uncertainties of the present study: $S_{eff} \sim 64\ \text{m}^3 \times \text{s}^{-1}$ with $T_{pump} = 300$ K and neglecting Γ_{core} (section 4.2). This might motivate the lack of a clear dependence on S_{eff}.

However, it is remarkable that a similar value of S_{eff}—which factors in the contribution of the wall—is experimentally observed for detached cases in TCV [167], MAST-U [114], and AUG[14] [14, 96, 123, 168], and even for the attached scenarios of Kallenbach *et al* [42]. Consistent behaviour is also found in simulations of EU-DEMO [144, 169] and ITER [28, 131, 151, 153, 170, 171], which follow the same trend. Crucially, across the entire ITER database, a fixed pump capture coefficient of 0.72% is adopted to explicitly reflect the realistic engineering constraint of $S_{eff} \sim 60\ \text{m}^3 \times \text{s}^{-1}$ [29].

The only exceptions are *simulated* cases in TCV [156], AUG [153], and DTT [26], which deviate by up to a factor ∼5 (DOD>1). Here a role might be played by both physical effects (e.g. plasma drifts not implemented or intrinsic code limitations [76, 77]) and geometric factors (e.g. the specific divertor location at which p_{div} was sampled). Additional contributors likely include the *estimated* wall recycling coefficients [156], and/or the *prescribed* pump capture coefficient. For instance, in AUG [153] the capture coefficient is not reported and thus cannot be assumed to correspond to the engineering S_{eff}. Instead, in DTT [26], an 8% capture coefficient was adopted—a value falling within the range identified by Tantos *et al* [163] in the same machine, but for different underlying edge plasma simulations.

The temperature T_{pump} is also not systematically documented. It, however, influences p_{div} according to equation (14) and could vary with the pump duct location in the simulated domain [10]—which does not usually include the entire sub-divertor volume [166, 172]. This further complicates the interpretation, alongside the complexities discussed by Yang *et al* [156] in their equations (2–3).

While numerical models have advanced considerably, capturing both pumping performance and plasma parameters simultaneously remains challenging [28]. These outliers are better interpreted as the consequence of differing modelling assumptions and boundary conditions.

Overall, the mild variation of S_{eff} across devices remains a striking feature—possibly reflecting the operator bias (section 4.1), whereby the community has converged on an effective pumping configuration (including the wall) that enables proficient operation within engineering and physical constraints.

These observations are here reported as such—dedicated first-principle investigations [163, 164], together with new experimental characterisations, will be needed to further comment on the matter.

4.4. Geometry

4.4.1. Divertor volume over plasma volume. Although a growth of Γ_D with the plasma volume V_p would be intuitive, the present data suggest that the divertor volume V_{div} actually dictates the correlation (equation (4)). Indeed, the WEST ('WE') tokamak is characterised by a peculiarly small V_{div}/V_p ratio if compared to its peers (see, e.g. figure 1 in [15]). As a result, WEST simultaneously appears (i) consistent with other devices in figure 3(*a*) ($V_{div} \sim 0.1\ \text{m}^3$), and (ii) as a notable outlier[15] when V_p is considered instead (not shown)—in fact down to a factor 40 below the average trend. Therefore,

[14] Some data might also be included in [42].

[15] COMPASS also features a WEST-like V_{div}/V_p ratio but no Q puff rate could be found in the literature.

either WEST is an anomaly within the entire family of magnetic confinement fusion devices, or V_{div} is the leading metric. Evidence suggest the latter is the case, as divertor-specific geometrical parameters provide better correlations than plasma-specific ones throughout the study.

Brida *et al* [173] demonstrate a correlation between the divertor radial extent (function of L_{div} and H_{div} herein) and the power fall-off length in the divertor private-flux region. This might explain a physical reason behind the above findings—transport from scrape-off layer to private-flux region.

4.4.2. Magnetic field geometry: the case of advanced divertor configurations (ADCs). Of appeal for future reactor designs, ADCs [64, 65, 174] optimise the poloidal/total flux expansion $f_{\mathrm{X,R}}$, grazing angle $\theta_{\perp}$ and parallel connection length L_{conn} to ameliorate the power exhaust challenge.

One such example is AUG's compact radiative divertor (CRD) of Lunt *et al* [65], which approaches the geometrical limit $\lim_{a\to 0}(S_{\mathrm{div}}/V_{\mathrm{div}}) \sim \lim_{a\to 0}(8.3/a) = +\infty$ (via equation (2)) and pushes equation (5) to $\lim_{a\to 0}\Gamma_{\mathrm{D}} = 0$. Although n_{sep} data are not available in [65], the CRD's $\Gamma_{\mathrm{D}} \sim 0.4\times10^{22}$ el $\times$ s^{-1} sits at the lower end of the AUG's range in the present database ($\sim 2.0\times10^{22}$ el $\times$ s^{-1}, on average) and, thus, is not inconsistent with the higher $S_{\mathrm{div}}/V_{\mathrm{div}}$ of the CRD.

Because the CRD's flux expansion approaches $+\infty$ in parallel to the divertor surface-to-volume ratio, $S_{\mathrm{div}}/V_{\mathrm{div}}$ can be thought as representing a proxy for the flux expansion. However, this does not apply at large, as the flux expansion can be magnetically tuned independently of $S_{\mathrm{div}}/V_{\mathrm{div}}$ (according to the definition in equation (1)). All of the above affect the detachment onset—but it is not directly captured by the simplistic divertor approximation in figure 1.

Still, any effect mediated by n_{sep} would be indirectly accounted for by the density dependences of equations (5) and (7), at least partially. Let us consider the DOD = 1 MAST-U cases from Moulton *et al* [128] in table 2. The density drop from #25 (conventional divertor, $n_{\mathrm{sep}} = 6.0\times10^{18}$ m^{-3}) to #26 (Super-X ADC, $n_{\mathrm{sep}} = 3.3\times10^{18}$ m^{-3}) illustrates the facilitated detachment access via the Super-X ADC. The accompanying decrease in Γ_{D} from 4.0×10^{21} el $\times$ s^{-1} to 0.5×10^{21} el $\times$ s^{-1} is partially captured by equation (5) (OPQ) (from 2.2×10^{21} el $\times$ s^{-1} to 1.4×10^{21} el $\times$ s^{-1}), but a difference persists—hence hinting at the role played by the unaccounted geometrical variables (e.g $\{f_{\mathrm{R,X}};\ \theta_{\perp};\ L_{\mathrm{conn}}\}$).

Though not accomplished at this stage for reasons of data unavailability, explicitly including the above-mentioned variables is expected to enhance the predictive capability for ADCs. Similar arguments hold for variations of the size of edge islands in stellarators [175, 176].

4.4.3. Other geometrical features. Including the effect of further low-level geometric features—such as divertor closure [177], puffing location [24], and vertical/horizontal target arrangement [178]—into high-level scaling laws remains a challenging task.

A useful proxy for divertor closure may be given by the ratio $L_{\mathrm{div}}/(2d_{\mathrm{Xpt}})$, where d_{Xpt} denotes the distance between the X-point and the closest wall element (not in the PFR). According to this metric: (i) in the limit $d_{\mathrm{Xpt}} \to 0$, closure becomes absolute (∞, i.e. the wall intersects the X-point); (ii) closure equals unity when $d_{\mathrm{Xpt}} = L_{\mathrm{div}}/2$; and (iii) closure is <1 when $d_{\mathrm{Xpt}} > L_{\mathrm{div}}/2$, corresponding to a very open divertor configuration (e.g. TCV [59, 81]). Within this framework, Γ_{D} would be expected to scale with $L_{\mathrm{div}}/(2d_{\mathrm{Xpt}})$ raised to a negative exponent (i.e. more closure implies smaller puffing to achieve DOD = 1). Another approach for TCV is reported in [179, 180].

The influence of the divertor dome could, in principle, be captured by subtracting its volume from V_{div}, a correction that can be implemented when machine CAD data and/or edge plasma simulations are available.

Regarding the puffing location, Osawa *et al* [24] (figure 7, bottom left, in conjunction with their table 2) report a measurable variation of n_{sep} with injection position—albeit within the range of the present uncertainties. Such dependence might explain the clustering of STEP (ST) data in figure 3(*b*) of this work. However, a method to include varying puffing locations into multi-machine scaling laws is currently lacking.

Similarly to the discussion in the previous section, these examples illustrate that while the inclusion of detailed geometric effects in global scalings is, in principle, feasible, it is not straightforward and will require further dedicated effort.

4.4.4. Limited plasma geometry. Plasma ramp-ups most commonly rely on an initial phase of limited plasma which can last several seconds [181], and therefore require dedicated assessments because of the significant loads involved [182]. Limited plasmas are not included in the current study as the leading dependences involve divertor parameters (section 4.4.1).

It is however noted that, for similar *plasma* volumes, Γ_{D} puffing rates in detached limited plasmas can be within a factor 2 of diverted ones. TFTR [183] compared to AUG [65, 139] and to WEST [147, 149], and J-TEXT [140] compared to JFT-2M [48] and to TCV [184] are two such examples.

Including geometrical variables depending on the magnetic field (section 4.4.2) to avoid any divertor-related parameters would be worthwhile investigating for limited plasmas.

4.5. Exclusion of liquid lithium cases

Despite the interest shown by the community [185, 186], edge plasma simulations featuring liquid lithium plasma-facing components were discarded from the present study. We did not succeed in accounting for data from the insightful collection of works of Emdee *et al* [187–190] for NSTX-U and of Islam *et al* [27, 191] for FNSF—which invariably figured as outliers, despite having achieved detached conditions.

Such studies do cover, as a whole, a wide range of operational scenarios for a spherical and a conventional tokamak, respectively, and different liquid lithium models. Therefore, a possible cause of their unique behaviour could be the lithium-driven lower recycling—herein unaccounted for as a variable,

but impacting on S_{eff} (section 4.3). Also potentially influential is lithium being an intrinsic impurity whose generation rate is dictated by the plasma, and not an externally-controlled extrinsic impurity.

Therefore, only the scoping studies of Islam *et al* [27, 191] not including lithium were here retained.

4.6. Lack of correlation with power

The divertor metrics which quantify the power exhaust challenge P_{sep}/R_0, $P_{\text{sep}}B_{\text{tor}}/R_0$ and $P_{\text{sep}}B_{\text{tor}}/R_0/n_{\text{sep}}^2$ [137] do depend on plasma, rather than divertor, geometry. Additionally, n_{sep} does not depend on heating power for a given Γ_{D} [42, 106]. Therefore, the leading dependence on divertor, and not plasma, volume (section 4.4.1) might be the reason why such P_{sep}-dependent divertor metrics fall short of correlating to the data better than, or even to the same degree of, equations (5) and (7). The limited availability of P_{sep} data might also be playing a role, and including P_{sep} in the scaling laws would still be worthwhile pursuing.

4.7. Applicability across different scenarios

The effect of a drastic change in opaqueness within a device is exemplified by the W7-AS stellarator ('WA') in figures 3(*b*) and 7(*a*). Γ_{D} data from McCormick *et al* [192] more than double from the average value of 0.6×10^{21} el $\times$ s^{-1} in the low-density simil-L-mode regime (termed 'normal confinement' [192], at abscissa $\sim 1 \times 10^{20}$), to 1.5×10^{21} el $\times$ s^{-1} in the high-density simil-H-mode ones ('improved confinement', at $\sim 7 \times 10^{20}$).

Equations (5) and (7) are also able to capture the smooth variation between L- and H-modes across all the other devices within figures 7(*a*) and 7(*b*), respectively. This is quantitatively confirmed by the validation in table 2. For impurity puffing, a 20% maximum deviation from H- to L-mode is expected, on paper, from equation (11) and its factor $(f^{\text{S}})^{-0.27}$.

Other concepts contemplated for future reactors [3, 137] are the I-mode [193, 194] and the negative triangularity [195]. On the one hand, Γ_{D} data are not available in the I-modes of Reinke *et al* [196], and only one instance of negative triangularity exists in the database—that of Mombelli *et al* [197] (DOD>1). On the other hand, the L-mode-like particle confinement of the former [198], and the L-mode-like pedestal absence of the latter [199] suggest that the present results might also hold for I-modes and negative triangularity plasmas.

4.8. The essence of GES for impurity seeding

Figure 8 pictorially illustrates the effect of the simplifications operated in section 3.3.1 to retrieve the GES impurity seeding rate $\Gamma_{\text{Z}}^{\text{GES}}$: (i) in its present form, GES only applies for DOD $= 1$ cases (black) while the reminder of the database (white, DOD>1) remains not sorted; (ii) although $\Gamma_{\text{Z}}^{\text{GES}}$ follows a standard multiplicative functional form, (i) implies

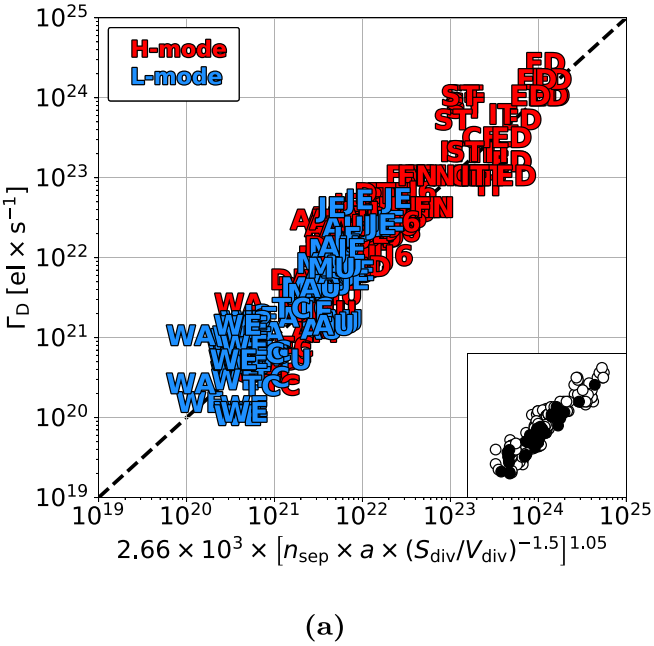

(a)

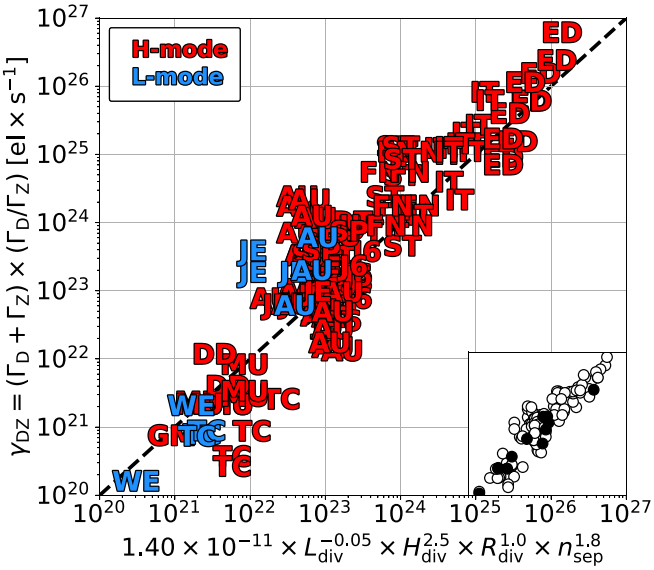

(b)

Figure 7. Analogous of figure 3(*b*) for equation (5), and of figure 4(*b*) for equation (7), but with the colouring which reflects the confinement regime.

that attempts at finding such a correlation via linear regression are futile—and the approach based on γ_{DZ} is required (section 3.2.2); therefore, (iii) conversely to Γ_{D} for which a scaling law could be directly found, Γ_{Z} is indissolubly tied to DOD.

In conclusion, the physics-driven approach provided access to a region of the parameter space inaccessible to a purely-empirical regression.

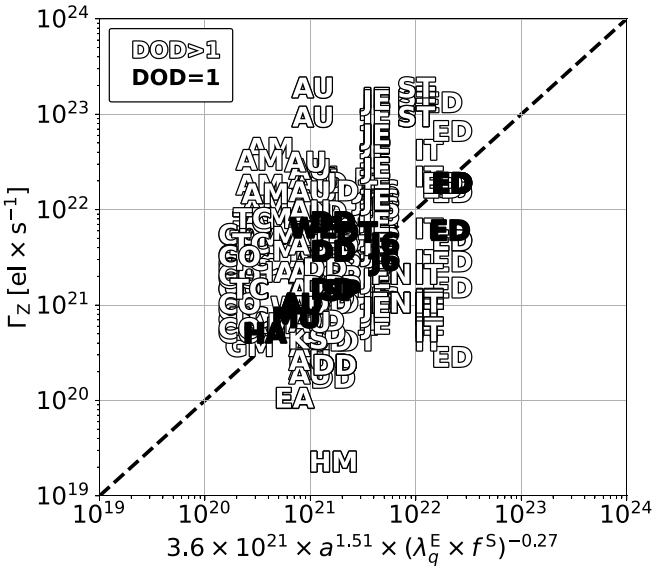

Figure 8. Graphical representation of Γ_Z^{GES} in equation (11), Greenwald–Eich–Scarabosio simplification of the scaling law for the impurity puffing rate. DOD = 1 points (black) follow the scaling whereas the others do not, hence clarifying on the power of a physics-driven approach.

Table 3. Applications of the scaling laws to conceptual power plants in the shape of tokamaks and stellarators (asterisked).

	ID	ARC [3]	MANTA [137]	Infinity Two* [30]	Stellaris* [31]	FNSF [27]
Actual Γ_D	—	—	—	—	—	4.0×10^{22}
Equation (4)	VOL	1.2×10^{23}	1.1×10^{23}	3.2×10^{22}	9.5×10^{21}	1.0×10^{22}
Equation (5)	OPQ	1.5×10^{23}	1.4×10^{23}	1.0×10^{23}	2.1×10^{21}	4.8×10^{22}
Equation (9)	HDL	—	—	—	—	1.9×10^{22}
Equation (10/12*)	GES/Su*	1.7×10^{23}	1.5×10^{23}	1.3×10^{23}	2.2×10^{23}	4.4×10^{22}
Actual Γ_Z	—	—	—	—	—	1.0×10^{21}
Equation (8)	via γ_{DZ}	7.7×10^{21}	2.2×10^{21}	9.5×10^{20}	5.4×10^{20}	2.7×10^{21}
Equation (11/13*)	GES/Su*	4.8×10^{21}	4.9×10^{21}	5.2×10^{21}	6.3×10^{21}	3.4×10^{21}

4.9. Practical examples

Table 3 exemplifies the application of the scaling laws to conceptual power plants, hence predicting a combination of Γ_D and Γ_Z sufficient to establish detachment (DOD = 1)—with the exception of FSNF.

DOD>1 cases for FNSF have already been thoroughly modelled. However, in the words of the author, Islam *et al* [27]: 'SOLPS is employed to identify the puffing and pumping levels [...]. Through an *extensive set of scans*, it has been determined that a combination of Ne seeding (1×10^{20} atoms s^{-1}) and D_2 puffing (4×10^{22} atoms s^{-1}) meets all the FNSF demands [...]' (italics added). In this instance (of, perhaps, DOD$\gtrsim$1) the values predicted for FNSF fall reasonably close to those found by the 'extensive set of scans', and could have aided a multi-parameter scan which instead lasted a few months [200]. A reasonable match with a case of DOD>1 via scaling laws valid for DOD = 1 is, however, not generalisable, as suggested by the violation of both HDL and GES upper bounds in table 3 (last column).

As for the other devices (yet to be thoroughly modelled), the stellarators Infinity Two [30] and Stellaris [31] differ from the perspective of Γ_D because of the expected n_{sep} = 10^{20} m^{-3} for the former and 10^{19} m^{-3} for the latter. Although a Stellaris-like disparity from the output of equation (4) to that of equation (5) is not unprecedented (e.g. #17 in table 2), these results caution on the impact of n_{sep} on the puffing rates and, ultimately, on the TFC [17, 18].

5. Conclusions

A database gathering a representative collection of stably detached edge plasmas has been assembled, and the engineering actuators of fuel Γ_D and impurity Γ_Z puffing rates investigated across magnetic confinement fusion devices. The inherent errors of experimental and numerical nature, alongside the confounding factor of the unquantified DOD, force the devisal of a robust strategy—to build scaling laws on the sub-set of instances past the detachment onset (DOD>1) and validate against cases specifically at the onset itself (DOD = 1)—the only truly comparable ones.

While scoping DOD>1 data for scaling laws, the divertor volume is found to broadly determine the fuel puffing rate across all the machines, in fact encompassing most of the machine-specific details and operational variations—from

desk-size linear plasma devices, through present-day stellarators and to future conventional and spherical tokamak pilot reactors.

Refinement of this geometry-centred scaling law sees the appearance of the opaqueness at the outer mid-plane separatrix. With the addition of empirical calibration factors to an otherwise physics-based law, the inclusion of opaqueness unifies the behaviour by accounting for devices featuring an exceptional density (e.g. high-field tokamaks)—and that are accompanied by exceptional fuelling as a consequence.

In regards to the impurity puffing rate, none of the above applies. Γ_Z is equally not correlated to geometry, opaqueness nor to any of the divertor metrics of the P_{sep}/R_0 family nor combination of. Motivated by the difference in the fuelling-seeding relationship between small and big devices, the non-linear variable $\gamma_{DZ} = (\Gamma_D + \Gamma_Z) \times (\Gamma_D/\Gamma_Z)$ is defined. And a linear regression for γ_{DZ} does satisfactorily order the data-points, thus providing a route to the estimation of Γ_Z, with Γ_D being known on the ground of previous findings.

The above suffices in fully characterising the engineering actuators both in L- and H-mode plasmas at DOD $= 1$. However, the uncertainty involved in and the level of detail set by the separatrix electron density beg for simplification. By leveraging density limits, minimalistic laws as a function of machine design parameters—and of scalings for the power fall-off length at most—are established.

Finally, the validation of the laws discovered is conducted on the DOD $= 1$ set of data—and it is successful. Refining the Γ_D scaling with the addition of opaqueness means that 43% (13/30) of the available predicted values falls within a factor 1.5 of the actual value, 63% (19/30) within a satisfactory factor 3, and the leftovers within a factor 6—while all respecting the GES strict upper bound Γ_D^{GES}. The H/L density limit is also shown to offer predictive capability for H-mode tokamak plasmas, accurate within a factor 2.3 and not depending on density.

Scaling laws involving impurity seeding also successfully validate, modulo the reduced data availability. The simplified GES law Γ_Z^{GES} is found to outperform the original, non-linear version—in fact leading to 50% of the predictions to match within a factor 1.5 (7/14), 29% within a factor 3 (4/14).

In conclusion, the present study demonstrates that a suitable combination of engineering actuators sufficient to access detachment can be accurately predicted for a given machine, on average within a factor 2. Moreover, simulations of future pilot plants are found to follow the extrapolations of present-day experimental data, hence adding on the confidence in the values predicted.

The laws determined find immediate applicability in system codes and high-level scoping studies, alongside providing guidance in low-level edge plasma modelling—to ultimately enable the rapid conceptual design and sizing of an appropriate TFC architecture and particle exhaust systems.

What these laws do *not* guarantee is an accurate description of the microscopic behaviour within a given device. Instead, they offer a macroscopic view across multiple machines, capturing system-level trends rather than machine-specific dynamics.

In perspective, contributions to expand/refine/revise the database (available at [46]) are *strongly encouraged*. This would enable a better characterisation of the categories under-represented in the validation, which would be needed to assess the applicability of the laws to spherical tokamaks (impurity-wise and at the inner target), linear plasma devices, and advanced divertor configurations in general. Because the corresponding DOD>1 data tend to follow the others, an extension of our scaling laws should apply for these cases. For the excluded liquid lithium cases an *ad hoc* approach would instead need development.

Though intriguing, further speculations about the relationship between divertor neutral pressure, puffing, and pumping across devices is not possible at this stage. Nevertheless, this interplay—together with the potential influence of the operator bias—remains an important subject for future dedicated work.

Our forthcoming studies focus on designing new laws descriptive of the behaviour of the individual machine. Additionally, in parallel to investigating the physical reasons behind the laws uncovered, revisiting the present results by accounting for the DOD would give the opportunity to predict puffing rates for scenarios more deeply detached (DOD>1)—near reactor-relevancy. Whether including a quantification of 'complete' detachment and/or MARFEs would allow to set an absolute inviolable limit to puffing rates remains to be seen.

Acknowledgments

This work has been (part-) funded by the EPSRC Energy Programme (Grant Number EP/W006839/1).

The authors would like to acknowledge the diligence of their colleagues across the scientific community for meticulously reporting valuable data in their publications.

J.D. Lore, E. Tinacba, O. Myatra, K. Verhaegh, M.S. Islam, J. Brownfield, M. Wigram and A. Kallenbach are also warmly thanked for providing useful pieces of information during the development of this work, and so are the teams of ASDEX Upgrade and UKAEA for the constructive feedbacks during seminars.

Stimulating discussions with T. Eich and D. Silvagni that helped interpreting the results deserve being emphatically acknowledged.

Last but not least, a special thank goes to S. Cirone (RUP) and C. Soika (Comm. Rex) for the ever-present support.

Appendix. Nomenclature and sources

Table 4 reports the machines figuring in the study, their unique ID and the scientific papers where data have been extracted from.

Table 4. Machine, corresponding ID and references used in the work.

#	Machine	ID	References
1	Alcator C-Mod	AM	[68, 90, 196, 201–203]
2	AUG	AU	[14, 42, 65, 70, 95, 96, 123, 139–141, 151–153, 168, 204–209]
3	CFETR	CF	[142]
4	COMPASS	CO	[62, 130, 210]
5	DIII-D	DD	[74, 89, 122, 211–217]
6	DT-ALPHA	DA	[124]
7	DTT	DT	[26, 76, 77, 218]
8	EAST	EA	[219–221]
9	EU-DEMO	ED	[67, 143, 144, 169, 222]
10	FNSF	FN	[27, 191]
11	Globus-M2	GM	[223]
12	HL-2A	HA	[47]
13	HL-2M	HM	[71, 224]
14	ITER	IT	[28, 131, 170, 171]
15	JET	JE	[72, 92, 94, 145, 225–232]
16	JFT-2M	J2	[48]
17	JT-60SA	J6	[25, 119, 233]
18	KSTAR	KS	[234]
19	LHD	LH	[51, 235, 236]
20	Magnum-PSI	MP	[52]
21	MAP-II	MI	[53]
22	MAST-U	MU	[61, 97, 114, 128, 237, 238]
23	NSTX	NS	[49, 127, 239, 240]
24	NSTX-U	NU	[69]
25	Pilot-PSI	PP	[60]
26	SPARC	SP	[50]
27	STEP	ST	[24, 241]
28	TCV	TC	[59, 99, 146, 147, 156, 167, 184, 197, 242–244]
29	TPD-Sheet IV	TS	[125, 245]
30	W7-AS	WA	[192]
31	W7-X	WX	[66, 246]
32	WEST	WE	[15, 148, 149, 247]

ORCID iDs

M. Moscheni 0000-0002-6355-7274
S. Lazerson 0000-0001-8002-0121
F. Levi 0000-0002-9971-9116
M. Siccinio 0009-0006-7870-6769
C. Tantos 0000-0003-1382-2364

References

[1] Federici G. *et al* 2019 Overview of the DEMO staged design approach in Europe *Nucl. Fusion* **59** 066013
[2] Meyer H. 2024 Plasma burn-mind the gap *Phil. Trans. R. Soc. A* **382** 20230406
[3] Sorbom B. *et al* 2015 ARC: a compact, high-field, Fusion Nuclear Science Facility and demonstration power plant with demountable magnets *Fusion Eng. Des.* **100** 378–405
[4] Warmer F. *et al* 2024 Overview of European efforts and advances in Stellarator power plant studies *Fusion Eng. Des.* **202** 114386
[5] Donné A. 2019 The European roadmap towards fusion electricity *Phil. Trans. R. Soc. A* **377** 2141
[6] Krieger K. *et al* 2025 Scrape-off layer and divertor physics: chapter 5 of the special issue: on the path to tokamak burning plasma operation *Nucl. Fusion* **65** 043001
[7] Stangeby P. 2000 *The Plasma Boundary of Magnetic Fusion Devices (Series in Plasma Physics and Fluid Dynamics)* (Taylor & Francis) (available at: https://books.google.co.uk/books?id = qOliQgAACAAJ)
[8] Zohm H. *et al* 2013 On the physics guidelines for a tokamak DEMO *Nucl. Fusion* **53** 073019
[9] Pitts R. *et al* 2017 Physics conclusions in support of ITER W divertor monoblock shaping *Nucl. Mater. Energy* **12** 60–74
[10] Henderson S. *et al* 2024 An overview of the STEP divertor design and the simple models driving the plasma exhaust scenario *Nucl. Fusion* **65** 016033
[11] Federici G., Biel W., Gilbert M.R., Kemp R., Taylor N. and Wenninger R. 2017 European DEMO design strategy and consequences for materials *Nucl. Fusion* **57** 092002
[12] Krasheninnikov S.I. and Kukushkin A.S. 2017 Physics of ultimate detachment of a tokamak divertor plasma *J. Plasma Phys.* **83** 155830501
[13] Soukhanovskii V.A. 2017 A review of radiative detachment studies in tokamak advanced magnetic divertor configurations *Plasma Phys. Control. Fusion* **59** 064005
[14] Henderson S. *et al* 2023 Divertor detachment and reattachment with mixed impurity seeding on ASDEX Upgrade *Nucl. Fusion* **63** 086024
[15] Yang H. *et al* 2024 Numerical study of a general criterion for divertor detachment control *Nucl. Fusion* **64** 106039
[16] Park J.-S., Lore J.D., Reinke M., Kuang A.Q., De Pascuale S. and Creely A. 2024 Full time-dependent SOLPS-ITER simulation of the SPARC tokamak: actuator design for

particle and divertor condition control *Nucl. Fusion* **64** 076036
[17] Abdou M., Riva M., Ying A., Day C., Loarte A., Baylor L.R., Humrickhouse P., Fuerst T.F. and Cho S. 2020 Physics and technology considerations for the deuterium–tritium fuel cycle and conditions for tritium fuel self sufficiency *Nucl. Fusion* **61** 013001
[18] Meschini S., Ferry S.E., Delaporte-Mathurin R. and Whyte D.G. 2023 Modeling and analysis of the tritium fuel cycle for ARC- and STEP-class D-T fusion power plants *Nucl. Fusion* **63** 126005
[19] Bonnin X., Dekeyser W., Pitts R., Coster D., Voskoboynikov S.W.S. and WIESEN S. 2016 Presentation of the new SOLPS-ITER code package for tokamak plasma edge modelling *Plasma Fusion Res.* **11** 1403102
[20] Kotov V. 2007 Numerical study of the ITER divertor plasma with the B2-EIRENE code package *PhD Thesis* Bochum University https://inis.iaea.org/records/kdt7v-xm516
[21] Rivals N., Tamain P., Marandet Y., Bonnin X., Bufferand H., Pitts R.A., Falchetto G., Yang H. and Ciraolo G. 2022 SOLEDGE3X full vessel plasma simulations for computation of ITER first-wall fluxes *Contrib. Plasma Phys.* **62** e202100182
[22] Simonini R., Corrigan G., Radford G., Spence J. and Taroni A. 1994 Models and numerics in the multi-fluid 2-D edge plasma code EDGE2D/U *Contrib. Plasma Phys.* **34** 368–73
[23] Reiter D. 2019 The EIRENE code user manual (available at: http://www.eirene.de/eirene.pdf)
[24] Osawa R., Newton S.L., Moulton D., Henderson S.S., Badicel V. and Hudoba A. 2024 Assessment of the impact of fuelling puff location on divertor impurity compression and enrichment in STEP *Nucl. Fusion* **64** 106007
[25] Rubino G., Calabrò G. and Wischmeier M. 2021 Assessment of scrape-off layer and divertor plasma conditions in JT-60SA with tungsten wall and nitrogen injection *Nucl. Mater. Energy* **26** 100895
[26] Balbinot L., Rubino G. and Innocente P. 2021 Development of DTT single null divertor scenario *Nucl. Mater. Energy* **27** 100952
[27] Islam M., Lore J., Smolentsev S., Kessel C. and Maingi R. 2024 Analysis and design of fast flow liquid Li divertor for Fusion Nuclear Science Facility (FNSF) using coupled plasma boundary and LM MHD/heat transfer codes *Nucl. Fusion* **64** 056036
[28] Lore J., Bonnin X., Park J.-S., Pitts R. and Stangeby P. 2022 High gas throughput SOLPS-ITER simulations extending the ITER database to strong detachment *Nucl. Fusion* **62** 106017
[29] Pitts R. *et al* 2019 Physics basis for the first ITER tungsten divertor *Nucl. Mater. Energy* **20** 100696
[30] Bader A. *et al* 2025 Power and particle exhaust for the infinity two fusion pilot plant *J. Plasma Phys.* **91** E67
[31] Lion J. *et al* 2025 Stellaris: a high-field quasi-isodynamic stellarator for a prototypical fusion power plant *Fusion Eng. Des.* **214** 114868
[32] Winters V.R. *et al* 2021 EMC3-EIRENE simulation of first wall recycling fluxes in W7-X with relation to H-alpha measurements *Plasma Phys. Control. Fusion* **63** 045016
[33] Saarelma S., Challis C.D., Garzotti L., Frassinetti L., Maggi C.F., Romanelli M. and Stokes C. 2017 Integrated modelling of H-mode pedestal and confinement in JET-ILW *Plasma Phys. Control. Fusion* **60** 014042
[34] Luda T., Angioni C., Dunne M.G., Fable E., Kallenbach A., Bonanomi N., Schneider P.A., Siccinio M. and Tardini G. 2020 Integrated modeling of ASDEX Upgrade plasmas combining core, pedestal and scrape-off layer physics *Nucl. Fusion* **60** 036023
[35] Kukushkin A., Pacher H.D., Pacher G.W., Janeschitz G., Coster D., Loarte A. and Reiter D. 2003 Scaling laws for edge plasma parameters in ITER from two-dimensional edge modelling *Nucl. Fusion* **43** 716
[36] Pacher H., Kukushkin A.S., Pacher G.W., Kotov V., Pitts R.A. and Reiter D. 2015 Impurity seeding in ITER DT plasmas in a carbon-free environment *J. Nucl. Mater.* **463** 591–5
[37] Dasbach S. and Wiesen S. 2023 Towards fast surrogate models for interpolation of tokamak edge plasmas *Nucl. Mater. Energy* **34** 101396
[38] Wiesen S. *et al* 2024 Data-driven models in fusion exhaust: AI methods and perspectives *Nucl. Fusion* **64** 086046
[39] Body T., Kallenbach A. and Eich T. 2025 A simple, accurate model for detachment access *Nucl. Fusion* **65** 086002
[40] Kallenbach A., Bernert M., Dux R., Reimold F. and Wischmeier M. 2016 Analytical calculations for impurity seeded partially detached divertor conditions *Plasma Phys. Control. Fusion* **58** 045013
[41] Siccinio M., Fable E., Lackner K., Scarabosio A., Wenninger R.P. and Zohm H. 2016 A 0D stationary model for the evaluation of the degree of detachment on the divertor plates *Plasma Phys. Control. Fusion* **58** 125011
[42] Kallenbach A., Sun H.J., Eich T., Carralero D., Hobirk J., Scarabosio A. and Siccinio M. 2018 Parameter dependences of the separatrix density in nitrogen seeded ASDEX Upgrade H-mode discharges *Plasma Phys. Control. Fusion* **60** 045006
[43] Cowley C., Lipschultz B., Moulton D. and Dudson B. 2022 Optimizing detachment control using the magnetic configuration of divertors *Nucl. Fusion* **62** 086046
[44] Silvagni D. *et al* 2025 Scaling of the H-mode electron separatrix density based on engineering parameters from C-Mod, AUG and JET data *Preprint: 2025 IAEA Fusion Energy Conf.* (*Chengdu,13–18 October 2025*) (available at: https://conferences.iaea.org/event/392/contributions/36007/)
[45] Goldston R.J., Reinke M.L. and Schwartz J.A. 2017 A new scaling for divertor detachment *Plasma Phys. Control. Fusion* **59** 055015
[46] Moscheni M. *et al* 2025 *[Database] Multi-Machine Scaling Laws for Fuel and Impurity Puffing Rates Sufficient for Detachment Access: A Systematic Review of Magnetic Confinement Fusion Devices* (available at: https://zenodo.org/records/15878965)
[47] Gao J. *et al* 2023 The effect of impurity seeding into the closed divertor on plasma detachment in the HL-2A tokamak *Nucl. Fusion* **63** 036006
[48] Kawashima H., Sengoku S., Ogawa T., Ogawa H., Uehara K., Miura Y. and Kimura H. (JFT-2M Group) 1999 Study of a closed divertor with strong gas puffing on JFT-2M *Nucl. Fusion* **39** 1679
[49] Meier E., Soukhanovskii V.A., Bell R.E., Diallo A., Kaita R., LeBlanc B.P., McLean A.G., Podestà M., Rognlien T.D. and Scotti F. 2015 Modeling detachment physics in the NSTX snowflake divertor *J. Nucl. Mater.* **463** 1200–4
[50] Lore J.D., Park J.-S., Eich T., Kuang A.Q., Reinke M.L., De Pascuale S., Lomanowski B., Creely A. and Canik J.M. 2024 Evaluation of SPARC divertor conditions in H-mode operation using SOLPS-ITER *Nucl. Fusion* **64** 126054
[51] Mukai K., Kawamura G., Masuzaki S., Hayashi Y., Tanaka H., Peterson B.J., Oishi T., Suzuki C., Kobayashi M. and Munechika K. 2022 Three-dimensional structure of radiative cooling in impurity seeded plasmas in the Large Helical Device *Nucl. Mater. Energy* **33** 101294
[52] Tanaka H., Hayashi Y., Kajita S., van der Meiden H.J., Yoshikawa M., Vernimmen J.W.M., Scholten J., Classen I., Morgan T.W. and Ohno N. 2020 Cross-field

transport in detached helium plasmas in Magnum-PSI *Plasma Phys. Control. Fusion* **62** 115021
[53] Okamoto A., Kado S., Iida Y. and Tanaka S. 2006 Comparison of Langmuir probe and laser Thomson scattering methods in the electron temperature measurement in divertor simulator MAP-II *Contrib. Plasma Phys.* **46** 416–21
[54] Bufferand H. *et al* 2017 Implementation of drift velocities and currents in SOLEDGE2D-EIRENE *Nucl. Mater. Energy* **12** 852–7
[55] Rognlien T., Milovich J., Rensink M. and Porter G. 1992 A fully implicit, time dependent 2-D fluid code for modeling tokamak edge plasmas *J. Nucl. Mater.* **196–198** 347–51
[56] Kawashima H., Shimizu K., Takizuka T., Sakurai S., Nakano T., Asakura N. and Ozeki T. 2006 Development of integrated SOL/divertor code and simulation study in JAEA *Plasma Fusion Res.* **1** 031–031
[57] Zagórski R., Telesca G. and Rapp J. (JET-EFDA Contributors) 2008 Integrated modelling of nitrogen seeded JET discharges *Contrib. Plasma Phys.* **48** 179–84
[58] Lipschultz B., LaBombard B., Marmar E.S., Pickrell M.M., Terry J.L., Watterson R., Wolfe S.M. 1984 Marfe: an edge plasma phenomenon *Nuclear Fusion* **24** 977–88
[59] Février O., Theiler C., Brida D., Colandrea C., De Oliveira H., Duval B.P., Galassi D., Gorno S., Henderson S., Komm M. 2021 Divertor closure effects on the TCV boundary plasma *Nucl. Mater. Energy* **27** 100977
[60] Hayashi Y., Ješko K., van der Meiden H.J., Vernimmen J.W.M., Morgan T.W., Ohno N., Kajita S., Yoshikawa M. and Masuzaki S. 2016 Plasma detachment study of high density helium plasmas in the Pilot-PSI device *Nucl. Fusion* **56** 126006
[61] Havlíčková E., Wischmeier M., Lipschultz B. and Fishpool G. 2015 The effect of the Super-X divertor of MAST Upgrade on impurity radiation as modelled by SOLPS *J. Nucl. Mater.* **463** 1209–13
[62] Komm M. *et al* 2019 Divertor impurity seeding experiments at the COMPASS tokamak *Nucl. Fusion* **59** 106035
[63] Reimerdes H. *et al* 2020 Assessment of alternative divertor configurations as an exhaust solution for DEMO *Nucl. Fusion* **60** 066030
[64] Militello F. *et al* 2021 Preliminary analysis of alternative divertors for DEMO *Nucl. Mater. Energy* **26** 100908
[65] Lunt T., Bernert M., Brida D., David P., Faitsch M., Pan O., Stieglitz D., Stroth U. and Redl A. 2023 Compact radiative divertor experiments at ASDEX Upgrade and their consequences for a reactor *Phys. Rev. Lett.* **130** 145102
[66] Effenberg F. *et al* 2019 First demonstration of radiative power exhaust with impurity seeding in the island divertor at Wendelstein 7-X *Nucl. Fusion* **59** 106020
[67] Zagórski R., Gałązka K. and Ivanova-Stanik I. 2016 Divertor power spreading in DEMO reactor by impurity seeding *Fusion Eng. Des.* **109–111** 37–41
[68] Lipschultz B. *et al* 1997 Modification and control of divertor detachment in Alcator C-Mod *J. Nucl. Mater.* **241–243** 771–6
[69] Chen Z.-P., Kotschenreuther M., Mahajan S. and Gerhardt S. 2018 A study of X-divertor in NSTX-U with SOLPS simulations *Nucl. Fusion* **58** 036015
[70] Senichenkov I.Y., Kaveeva E.G., Rozhansky V.A., Voskoboynikov S.P., Veselova I.Y., Shtyrkhunov N.V., Coster D.P. and Bonnin X. 2021 Approaching the radiating X-point in SOLPS-ITER modeling of ASDEX Upgrade H-mode discharges *Plasma Phys. Control. Fusion* **63** 055011
[71] Zhou Y., Zheng G., Du H., Li J. and Xue L. 2022 Predictive modeling of the deuterium gas puffing effect on impurity and heat flux compression for the HL-2M divertor by SOLPS *Fusion Eng. Des.* **182** 113222
[72] Guillemaut C. *et al* 2013 EDGE2D-EIRENE modelling of divertor detachment in JET high triangularity L-mode plasmas in carbon and Be/W environment *J. Nucl. Mater.* **438** S638–42
[73] LaBombard B. *et al* 2011 Scaling of the power exhaust channel in Alcator C-Mod *Phys. Plasmas* **18** 056104
[74] Lan H., Osborne T.H., Groebner R.J., Snyder P.B., Xu G.S., Grierson B.A., Victor B.S., Leonard A.W. and Wang H.Q. 2020 H-mode pedestal improvements with neon injection in DIII-D *Nucl. Fusion* **60** 056013
[75] Brunner D., Kuang A., LaBombard B. and Terry J. 2018 The dependence of divertor power sharing on magnetic flux balance in near double-null configurations on Alcator C-Mod *Nucl. Fusion* **58** 076010
[76] Moscheni M. *et al* 2022 Cross-code comparison of the edge codes SOLPS-ITER, SOLEDGE2D and UEDGE in modelling a low-power scenario in the DTT *Nucl. Fusion* **62** 056009
[77] Moscheni M. *et al* 2025 Cross-code comparison of the edge codes SOLPS-ITER, SOLEDGE2D and UEDGE in modelling a high-power neon-seeded scenario in the DTT *Nucl. Fusion* **65** 026025
[78] Eich T. *et al* 2013 Scaling of the tokamak near the scrape-off layer H-mode power width and implications for ITER *Nucl. Fusion* **53** 093031
[79] Scarabosio A., Eich T., Herrmann A. and Sieglin B. 2013 Outer target heat fluxes and power decay length scaling in L-mode plasmas at JET and AUG *J. Nucl. Mater.* **438** S426–30
[80] Sieglin B., Eich T., Faitsch M., Herrmann A. and Scarabosio A. 2016 Investigation of scrape-off layer and divertor heat transport in ASDEX Upgrade L-mode *Plasma Phys. Control. Fusion* **58** 055015
[81] Reimerdes H. *et al* 2022 Overview of the TCV tokamak experimental programme *Nucl. Fusion* **62** 042018
[82] Faitsch M., Maurizio R., Gallo A., Coda S., Eich T., Labit B., Merle A., Reimerdes H., Sieglin B. and Theiler C. 2018 Dependence of the L-Mode scrape-off layer power fall-off length on the upper triangularity in TCV *Plasma Phys. Control. Fusion* **60** 045010
[83] Eich T., Manz P., Goldston R.J., Hennequin P., David P., Faitsch M., Kurzan B., Sieglin B. and Wolfrum E. 2020 Turbulence driven widening of the near-SOL power width in ASDEX Upgrade H-Mode discharges *Nucl. Fusion* **60** 056016
[84] Goldston R. 2011 Heuristic drift-based model of the power scrape-off width in low-gas-puff H-mode tokamaks *Nucl. Fusion* **52** 013009
[85] Greenwald M., Terry J.L., Wolfe S.M., Ejima S., Bell M.G., Kaye S.M. and Neilson G.H. 1988 A new look at density limits in tokamaks *Nucl. Fusion* **28** 2199
[86] Eich T., Goldston R.J., Kallenbach A., Sieglin B. and Sun H.J. 2018 Correlation of the tokamak H-mode density limit with ballooning stability at the separatrix *Nucl. Fusion* **58** 034001
[87] Bernert M. *et al* 2014 The H-mode density limit in the full tungsten ASDEX Upgrade tokamak *Plasma Phys. Control. Fusion* **57** 014038
[88] Sudo S., Takeiri Y., Zushi H., Sano F., Itoh K., Kondo K. and Iiyoshi A. 1990 Scalings of energy confinement and density limit in stellarator/heliotron devices *Nucl. Fusion* **30** 11
[89] Mordijck S. 2020 Overview of density pedestal structure: role of fueling versus transport *Nucl. Fusion* **60** 082006
[90] Reksoatmodjo R., Mordijck S., Hughes J., Lore J. and Bonnin X. 2021 The role of edge fueling in determining the pedestal density in high neutral opacity Alcator C-Mod experiments *Nucl. Mater. Energy* **27** 100971

[91] Miller M., Hughes J.W., Rosenthal A.M., Mordijck S., Reksoatmodjo R., Wigram M., Dunsmore J., Sciortino F., Wilcox R.S. and Odstrčil T. 2025 Enhanced pedestal transport driven by edge collisionality on Alcator C-Mod and its role in regulating H-mode pedestal gradients *Nucl. Fusion* **65** 026029
[92] Telesca G. *et al* 2022 Core-SOL simulations of high-power JET-ILW pulses fuelled with gas and/or with pellets *Contrib. Plasma Phys.* **62** e202100186
[93] Moulton D. *et al* 2015 Pumping in vertical and horizontal target configurations on JET in L-mode; an interpretive study using EDGE2D-EIRENE *Proc. 42nd European Physical Society Conf. Plasma Physics (EPS 2015)* ed R. Bingham and P. Lisbon (https://doi.org/10.5445/IR/1000058762)
[94] Loarte A. *et al* 1998 Plasma detachment in JET Mark I divertor experiments *Nucl. Fusion* **38** 331
[95] Potzel S., Wischmeier M., Bernert M., Dux R., Müller H.W. and Scarabosio A. 2013 A new experimental classification of divertor detachment in ASDEX Upgrade *Nucl. Fusion* **54** 013001
[96] Kallenbach A. *et al* 2015 Partial detachment of high power discharges in ASDEX Upgrade *Nucl. Fusion* **55** 053026
[97] Verhaegh K. *et al* 2022 Spectroscopic investigations of detachment on the MAST Upgrade Super-X divertor *Nucl. Fusion* **63** 016014
[98] Feng Y., Kobayashi M., Lunt T. and Reiter D. 2011 Comparison between stellarator and tokamak divertor transport *Plasma Phys. Control. Fusion* **53** 024009
[99] Fil A., Lipschultz B., Moulton D., Dudson B.D., Février O., Myatra O., Theiler C., Verhaegh K. and Wensing M. 2020 Separating the roles of magnetic topology and neutral trapping in modifying the detachment threshold for TCV *Plasma Phys. Control. Fusion* **62** 035008
[100] Leonard A., McLean A., Makowski M. and Stangeby P. 2017 Compatibility of separatrix density scaling for divertor detachment with H-mode pedestal operation in DIII-D *Nucl. Fusion* **57** 086033
[101] Myatra O., Lipschultz B., Moulton D., Verhaegh K., Dudson B., Orchard S., Fil A. and Cowley C. 2023 Predictive SOLPS-ITER simulations to study the role of divertor magnetic geometry in detachment control in the MAST-U Super-X configuration *Nucl. Fusion* **63** 096018
[102] Thorburn W. 1915 Occam's razor *Mind* **XXIV** 287–8
[103] Fisher R.A. 1992 *Statistical Methods for Research Workers* (Springer) pp 66–70
[104] Ghoos K., Börner P., Dekeyser W., Kukushkin A. and Baelmans M. 2018 Grid resolution study for B2-EIRENE simulation of partially detached ITER divertor plasma *Nucl. Fusion* **59** 026001
[105] Boeyaert D., Carli S., Ghoos K., Dekeyser W., Wiesen S. and Baelmans M. 2022 Numerical error analysis of SOLPS-ITER simulations of EAST *Nucl. Fusion* **63** 016005
[106] Paradela Pérez I., Lomanowski B., Lore J.D., Lovell J. and Moulton D. 2025 Power balance and divertor asymmetries in the Super-X divertors of MAST-U using SOLPS-ITER *Nucl. Fusion* **65** 066026
[107] Wu H., Subba F., Wischmeier M. and Zanino R. 2020 Comparison of SOLPS5.0 and SOLPS-ITER simulations for ASDEX Upgrade L-mode *Contrib. Plasma Phys.* **60** e201900120
[108] Makarov S., Coster D.P., Kaveeva E.G., Rozhansky V.A., Senichenkov I.Y., Veselova I.Y., Voskoboynikov S.P., Stepanenko A.A., Bonnin X. and Pitts R.A. 2023 Implementation of SOLPS-ITER code with new Grad–Zhdanov module for D–T mixture *Nucl. Fusion* **63** 026014
[109] Wiesen S., Bonnin X. and Pitts R. 2025 Conclusive benchmark of SOLPS-ITER against the SOLPS4.3 ITER divertor design reference *Nucl. Fusion* **65** 056027
[110] Reimold F. *et al* 2015 Experimental studies and modeling of complete H-mode divertor detachment in ASDEX Upgrade *J. Nucl. Mater.* **463** 128–34
[111] Varoutis S., Gleason-González C., Moulton D., Kruezi U., Groth M., Day C., Wiesen S. and Harting D. 2017 Simulation of neutral gas flow in the JET sub-divertor *Fusion Eng. Des.* **121** 13–21
[112] Wiesen S. *et al* 2018 On the role of finite grid extent in SOLPS-ITER edge plasma simulations for JET H-mode discharges with metallic wall *Nucl. Mater. Energy* **17** 174–81
[113] Pan O., Bernert M., Lunt T., Cavedon M., Kurzan B., Wiesen S., Wischmeier M. and Stroth U. (the ASDEX Upgrade Team) 2022 SOLPS-ITER simulations of an X-point radiator in the ASDEX Upgrade tokamak *Nucl. Fusion* **63** 016001
[114] Henderson S. *et al* 2024 Validating reduced models for detachment onset and reattachment times on MAST-U *Nucl. Mater. Energy* **41** 101765
[115] Silvagni D. *et al* 2025 The separatrix electron density in JET, ASDEX Upgrade and Alcator C-Mod H-mode plasmas: a common evaluation procedure and correlation with engineering parameters *Nucl. Mater. Energy* **42** 101867
[116] Wigram M. 2024 Kinetic corrections to the 2-point-model and applications to predictions in SPARC and C-Mod *66th Annual Meeting of the APS Division of Plasma Physics* (American Physical Society) (https://meetings.aps.org/Meeting/DPP24/Session/TO06.13)
[117] Monk R. *et al* 1997 Interpretation of ion flux and electron temperature profiles at the JET divertor target during high recycling and detached discharges *J. Nucl. Mater.* **241–243** 396–401
[118] Ohno N., Tanaka N., Ezumi N., Nishijima D. and Takamura S. 2001 Influence of plasma resistance and fluctuation on probe characteristics in detached recombining plasmas *Contrib. Plasma Phys.* **41** 473–80
[119] De Gianni L. *et al* 2024 Core and edge modeling of JT-60SA H-mode highly radiative scenarios using SOLEDGE3X–EIRENE and METIS codes *Front. Phys.* **12** 1422286
[120] Oliveira D. *et al* 2022 Validation of edge turbulence codes against the TCV-X21 diverted L-mode reference case *Nucl. Fusion* **62** 096001
[121] Matthews G. 2013 Plasma operation with an all metal first-wall: comparison of an ITER-like wall with a carbon wall in JET *J. Nucl. Mater.* **438** S2–S10
[122] Wang H. *et al* 2023 Study on divertor detachment and pedestal characteristics in the DIII-D upper closed divertor *Nucl. Fusion* **63** 046004
[123] Kallenbach A. *et al* 2013 Impurity seeding for tokamak power exhaust: from present devices via ITER to DEMO *Plasma Phys. Control. Fusion* **55** 124041
[124] Yoshimura K., Takahashi H., Nishimura R., Hara T., Kagaya S., Oishi T., Matsuyama A. and Tobita K. 2025 Contribution of hydrogen molecular activated recombination to plasma particle loss in DT-ALPHA *Plasma Fusion Res.* **20** 1401015
[125] Onda T., Kajita S., Iijima T., Tonegawa A., Ohno N. and Tanaka H. 2017 Transverse motion of a plasma column in a sheet plasma *Contrib. Plasma Phys.* **57** 87–93
[126] Soukhanovskii V. *et al* 2007 Divertor heat flux reduction and detachment experiments in NSTX *J. Nucl. Mater.* **363–5** 432–6

[127] Soukhanovskii V. *et al* 2009 Divertor heat flux mitigation in high-performance H-mode discharges in the National Spherical Torus Experiment *Nucl. Fusion* **49** 095025
[128] Moulton D., Harrison J.R., Xiang L., Ryan P.J., Kirk A., Verhaegh K., Wijkamp T.A., Federici F., Clark J.G. and Lipschultz B. 2024 Super-X and conventional divertor configurations in MAST-U ohmic L-mode; a comparison facilitated by interpretative modelling *Nucl. Fusion* **64** 076049
[129] Chuang Y.-C., Mordijck S., Fitzpatrick R. and Reksoatmodjo R. 2025 SOLPS-ITER simulations to study the impact of aspect ratio on edge fueling neutrals in tokamaks *Nucl. Mater. Energy* **42** 101865
[130] Komm M. *et al* 2021 Power exhaust by core radiation at COMPASS tokamak *Nucl. Fusion* **61** 036016
[131] Veselova I., Kaveeva E., Rozhansky V., Senichenkov I., Poletaeva A., Pitts R.A. and Bonnin X. 2021 SOLPS-ITER drift modelling of ITER burning plasmas with narrow near-SOL heat flux channels *Nucl. Mater. Energy* **26** 100870
[132] Bufferand H. *et al* 2022 Implementation of multi-component Zhdanov closure in SOLEDGE3X *Plasma Phys. Control. Fusion* **64** 055001
[133] Casali L. *et al* 2014 Transport analysis of high radiation and high density plasmas in the ASDEX Upgrade tokamak *EPJ Web Conf.* **79** 01007
[134] Kallenbach A., Bernert M., Dux R., Eich T., Henderson S.S., Pütterich T., Reimold F., Rohde V. and Sun H.J. 2019 Neutral pressure and separatrix density related models for seed impurity divertor radiation in ASDEX Upgrade *Nucl. Mater. Energy* **18** 166–74
[135] Militello F. 2022 *Radiation and Detachment* (Springer) pp 313–86
[136] Scotti F. *et al* 2024 High performance power handling in the absence of an H-mode edge in negative triangularity DIII-D plasmas *Nucl. Fusion* **64** 094001
[137] Rutherford G. *et al* The MANTA Collaboration 2024 MANTA: a negative-triangularity NASEM-compliant fusion pilot plant *Plasma Phys. Control. Fusion* **66** 105006
[138] Greenwald M. 2002 Density limits in toroidal plasmas *Plasma Phys. Control. Fusion* **44** R27
[139] Brida D. *et al* 2017 Heat flux pattern in detached L-modes and ELM mitigated H-modes with rotating magnetic perturbations in ASDEX Upgrade *Nucl. Fusion* **57** 116006
[140] Wu H., Shi P., Subba F., Sun H., Wischmeier M. and Zanino R. 2023 SOLPS-ITER numerical evaluation about the effect of drifts in a divertor configuration of ASDEX-Upgrade and a limiter configuration of J-TEXT *Fusion Eng. Des.* **196** 114023
[141] Wu H., Subba F., Wischmeier M., Cavedon M. and Zanino R. 2021 SOLPS-ITER modeling of ASDEX Upgrade L-mode detachment states *Plasma Phys. Control. Fusion* **63** 105005
[142] Mao S., Guo Y., Peng X.B., Luo Z.P., Xiao B.J., Song Y.T., Yao D.M., Zhu S.Z. and Ye M.Y. 2015 Evaluation of target-plate heat flux for a possible snowflake divertor in CFETR using SOLPS *J. Nucl. Mater.* **463** 1233–7
[143] Aho-Mantila L. *et al* 2021 Scoping the characteristics and benefits of a connected double-null configuration for power exhaust in EU-DEMO *Nucl. Mater. Energy* **26** 100886
[144] Subba F., Coster D., Moscheni M. and Siccinio M. 2021 SOLPS-ITER modeling of divertor scenarios for EU-DEMO *Nucl. Fusion* **61** 106013
[145] Groth M. *et al* 2015 Divertor plasma conditions and neutral dynamics in horizontal and vertical divertor configurations in JET-ILW low confinement mode plasmas *J. Nucl. Mater.* **463** 471–6
[146] Harrison J. *et al* 2017 Detachment evolution on the TCV tokamak *Nucl. Mater. Energy* **12** 1071–6
[147] Yang H. 2023 Control of detachment in the divertor region of tokamaks: impact of wall geometry, particle, and energy sources *PhD Thesis* Aix-Marseille University 2023A hal-04133974v1 (available at: https://hal.science/hal-04133974v1)
[148] Rivals N. *et al* 2024 Experiments and SOLEDGE3X modeling of dissipative divertor and X-point radiator regimes in WEST *Nucl. Mater. Energy* **40** 101723
[149] Yang H. *et al* 2022 Numerical modelling of the impact of leakage under divertor baffle in WEST *Nucl. Mater. Energy* **33** 101302
[150] Lengyel L. 1981 Analysis of radiating plasma boundary layers, Max Planck Institute for Plasma Physics *Technical Report* 1/191
[151] Sytova E., Pitts R.A., Kaveeva E., Bonnin X., Coster D., Rozhansky V., Senichenkov I., Veselova I., Voskoboynikov S. and Reimold F. 2019 Comparing N versus Ne as divertor radiators in ASDEX-upgrade and ITER *Nucl. Mater. Energy* **19** 72–78
[152] Senichenkov I.Y., Kaveeva E.G., Sytova E.A., Rozhansky V.A., Voskoboynikov S.P., Veselova I.Y., Coster D.P., Bonnin X. and Reimold F. 2019 On mechanisms of impurity leakage and retention in the tokamak divertor *Plasma Phys. Control. Fusion* **61** 045013
[153] Senichenkov I., Poletaeva A.G., Kaveeva E.G., Veselova I.Y., Rozhansky V.A., Coster D., Bonnin X. and Pitts R.A. 2023 SOLPS-ITER modeling of Ar and N seeded discharges in ASDEX Upgrade and ITER *Nucl. Mater. Energy* **34** 101361
[154] Barrett T.R., Jones C., Blatchford P., Smith B., McAdams R. and Woods N. 2011 Engineering design of the double neutral beam injection system for MAST Upgrade *Fusion Eng. Des.* **86** 789–92
[155] Coda S. *et al* 2017 Overview of the TCV tokamak program: scientific progress and facility upgrades *Nucl. Fusion* **57** 102011
[156] Yang H. *et al* 2023 Numerical study of divertor detachment in TCV H-mode scenarios *Plasma Phys. Control. Fusion* **65** 125005
[157] Henderson S. *et al* 2019 An assessment of nitrogen concentrations from spectroscopic measurements in the JET and ASDEX Upgrade divertor *Nucl. Mater. Energy* **18** 147–52
[158] Henderson S. *et al* 2021 Parameter dependencies of the experimental nitrogen concentration required for detachment on ASDEX Upgrade and JET *Nucl. Mater. Energy* **28** 101000
[159] Kovari M., Kemp R., Lux H., Knight P., Morris J. and Ward D.J. 2014 PROCESS: a systems code for fusion power plants—part 1: physics *Fusion Eng. Des.* **89** 3054–69
[160] Horsten N. *et al* 2022 Validation of SOLPS-ITER simulations with kinetic, fluid and hybrid neutral models for JET-ILW low-confinement mode plasmas *Nucl. Mater. Energy* **33** 101247
[161] Schweinzer J., Sandmann W., Haas G., Neuhauser J., Murmann H. and Salzmann H. 1999 Comparison of scrape-off layer behaviour between DIV-I and DIV-II operations on ASDEX-Upgrade *J. Nucl. Mater.* **266–9** 934–9
[162] Varoutis S., Tantos C., Strobel H., Day C., Dhard C.P., Haak V., Igitkhanov Y. and Naujoks D. 2024 Numerical simulation of neutral gas dynamics in the W7-X sub-divertor *Nucl. Fusion* **64** 076011

[163] Tantos C., Varoutis S., Hauer V., Day C. and Innocente P. 2023 3D numerical study of neutral gas dynamics in the DTT particle exhaust using the DSMC method *Nucl. Fusion* **64** 016019
[164] Tantos C., Strobel H., Hauer V., Day C., Giegerich T. and Innocente P. 2025 Numerical investigation of the DTT cryopump performance via 3D direct simulation Monte Carlo modeling *Fusion Eng. Des.* **215** 115021
[165] Kukushkin A., Pacher H.D., Kotov V., Reiter D., Coster D.P. and Pacher G.W. 2007 Effect of the dome on divertor performance in ITER *J. Nucl. Mater.* **363–5** 308–13
[166] Pshenov A., Bonnin X. and Pitts R. 2025 SOLPS-ITER simulations of the ITER divertor with improved plasma-facing component geometry *Nucl. Mater. Energy* **42** 101851
[167] Février O. *et al* 2020 Nitrogen-seeded divertor detachment in TCV L-mode plasmas *Plasma Phys. Control. Fusion* **62** 035017
[168] Reimold F., Wischmeier M., Bernert M., Potzel S., Kallenbach A., Müller H.W., Sieglin B. and Stroth U. 2015 Divertor studies in nitrogen induced completely detached H-modes in full tungsten ASDEX Upgrade *Nucl. Fusion* **55** 033004
[169] Korzueva V., Kaveeva E., Vekshina E., Rozhansky V., Senichenkov I., Shirobokov A. and Coster D. 2023 SOLPS-ITER modeling of EU-DEMO Ar-seeded cases with drifts and kinetic neutrals *Plasma Phys. Control. Fusion* **65** 085009
[170] Sureshkumar S. *et al* 2024 First SOLEDGE3X-EIRENE simulations of the ITER neon seeded burning plasma boundary up to the first wall *Nucl. Mater. Energy* **41** 101780
[171] Kaveeva E. *et al* 2020 SOLPS-ITER modelling of ITER edge plasma with drifts and currents *Nucl. Fusion* **60** 046019
[172] Kaveeva E., Rozhansky V., Veselova I., Senichenkov I., Giroud C., Pitts R.A., Wiesen S. and Voskoboynikov S. 2021 SOLPS-ITER drift modelling of JET Ne and N-seeded H-modes *Nucl. Mater. Energy* **28** 101030
[173] Brida D., Grenfell G., Grover O., Silvagni D., Faitsch M. and Stroth U. 2025 Transport and profile broadening in the private flux region of ASDEX Upgrade and role for power exhaust *Nucl. Fusion* **65** 026065
[174] Lee K. *et al* 2025 *x*-point target radiator regime in tokamak divertor plasmas *Phys. Rev. Lett.* **134** 185102
[175] Feng Y., Beidler C.D., Geiger J., Helander P., Hölbe H., Maassberg H., Turkin Y. and Reiter D. 2016 On the W7-X divertor performance under detached conditions *Nucl. Fusion* **56** 126011
[176] Peterson B. *et al* 2025 Investigation of island size effect on radiation distribution during attached and detached plasmas in the island divertor of W7-X *Nucl. Mater. Energy* **42** 101868
[177] Cowley C., Moulton D. and Lipschultz B. 2024 Simulating the impact of baffling on divertor performance using SOLPS-ITER
[178] Loarte A. 2001 Effects of divertor geometry on tokamak plasmas *Plasma Phys. Control. Fusion* **43** R183
[179] Reimerdes H. *et al* 2023 Variable gas-baffling in the TCV divertor *29th IAEA Fusion Energy Conf. (FEC 2023)*, 2023, IAEA-CN-316
[180] Tonello E. *et al* 2025 Modelling divertor solutions for power exhaust: in-depth experimental validation in TCV *30th IAEA Fusion Energy Conf. (IAEA FEC 2025 Tianfu)* (*Tianfu International Convention Center, Chengdu, China, 13–18 October 2025*) (https://conferences.iaea.org/event/392/contributions/35725/)
[181] Pitts R. *et al* 2025 Plasma-wall interaction impact of the ITER re-baseline *Nucl. Mater. Energy* **42** 101854
[182] Kocan M. *et al* 2015 Impact of a narrow limiter SOL heat flux channel on the ITER first wall panel shaping *Nucl. Fusion* **55** 033019
[183] Bush C., Strachan J., and Schivell J. 1989 Neutral beam heating of detached plasmas in TFTR *Technical Report* (Princeton University) (https://inis.iaea.org/records/sc4zj-ex941)
[184] Harrison J.R. *et al* 2019 Progress toward divertor detachment on TCV within H-mode operating parameters *Plasma Phys. Control. Fusion* **61** 065024
[185] de Castro A., Moynihan C., Stemmley S., Szott M. and Ruzic D.N. 2021 Lithium, a path to make fusion energy affordable *Phys. Plasmas* **28** 050901
[186] Nallo G., Mazzitelli G., Moscheni M., Subba F. and Zanino R. 2022 SOLPS-ITER simulations of a CPS-based liquid metal divertor for the EU DEMO: Li vs Sn *Nucl. Fusion* **62** 036008
[187] Emdee E., Goldston R., Lore J. and Zhang X. 2021 Predictive modeling of a lithium vapor box divertor in NSTX-U using SOLPS-ITER *Nucl. Mater. Energy* **27** 101004
[188] Emdee E. and Goldston R. 2023 Comparing lithium vapor box designs in a high heat flux scenario using SOLPS-ITER *Nucl. Mater. Energy* **34** 101335
[189] Emdee E.D. and Goldston R.J. 2023 The effect of gas injection location on a lithium vapor box divertor in NSTX-U *Nucl. Fusion* **63** 096003
[190] Emdee E., Goldston R., Khodak A. and Maingi R. 2024 Optimization of lithium vapor box divertor evaporator location on NSTX-U using SOLPS-ITER *Nucl. Fusion* **64** 086047
[191] Islam M., Lore J., Smolentsev S. and Kessel C. 2022 Divertor geometry modeling with the SOLPS-ITER code for reactor concepts with liquid metal divertors *Nucl. Mater. Energy* **33** 101292
[192] McCormick K. *et al* 2002 New advanced operational regime on the W7-AS Stellarator *Phys. Rev. Lett.* **89** 015001
[193] Wagner F. *et al* 1982 Regime of improved confinement and high beta in neutral-beam-heated divertor discharges of the ASDEX tokamak *Phys. Rev. Lett.* **49** 1408–12
[194] Whyte D. *et al* 2010 I-mode: an H-mode energy confinement regime with L-mode particle transport in Alcator C-Mod *Nucl. Fusion* **50** 105005
[195] Austin M.E. *et al* 2019 Achievement of reactor-relevant performance in negative triangularity shape in the DIII-D tokamak *Phys. Rev. Lett.* **122** 115001
[196] Reinke M. *et al* 2019 Radiative heat exhaust in Alcator C-Mod I-mode plasmas *Nucl. Fusion* **59** 046018
[197] Mombelli F. *et al* 2025 Impact of triangularity on edge transport and divertor detachment: a SOLPS-ITER study of TCV L-mode plasmas (arXiv:2506.03966)
[198] Hubbard A.E. *et al* 2011 Edge energy transport barrier and turbulence in the I-mode regime on Alcator C-Mod *Phys. Plasmas* **18** 056115
[199] Marinoni A., Sauter O. and Coda S. 2021 A brief history of negative triangularity tokamak plasmas *Rev. Modern Plasma Phys.* **5** 1–65
[200] Islam M. 2025 Personal communication
[201] Lore J., Reinke M.L., LaBombard B., Lipschultz B., Churchill R.M., Pitts R.A. and Feng Y. 2015 EMC3-EIRENE modeling of toroidally-localized divertor gas injection experiments on Alcator C-Mod *J. Nucl. Mater.* **463** 515–8
[202] Lore J.D., Reinke M.L., Brunner D., LaBombard B., Lipschultz B., Terry J., Pitts R.A. and Feng Y. 2015 Three-dimensional simulation of H-mode plasmas with localized divertor impurity injection on Alcator C-Mod

using the edge transport code EMC3-EIRENE *Phys. Plasmas* **22** 056106
[203] Goetz J.A. *et al* 1999 High confinement dissipative divertor operation on Alcator C-Mod *Phys. Plasmas* **6** 1899–906
[204] Ivanova-Stanik I., Zagórski R., Chomiczewska A., Bernert M., Glöggler S. and Kallenbach A. 2022 COREDIV modelling of nitrogen and krypton seeding at the ASDEX Upgrade tokamak *Plasma Phys. Control. Fusion* **64** 045015
[205] Pan O. 2024 Power exhaust in future alternative divertor configurations for the ASDEX Upgrade tokamak *PhD Thesis* Technische Universität München fakultät für Physik
[206] Carralero D. *et al* 2017 A study on the density shoulder formation in the SOL of H-mode plasmas *Nucl. Mater. Energy* **12** 1189–93
[207] Bernert M. *et al* 2020 X-point radiation, its control and an ELM suppressed radiating regime at the ASDEX Upgrade tokamak *Nucl. Fusion* **61** 024001
[208] Bernert M. *et al* 2017 Power exhaust by SOL and pedestal radiation at ASDEX Upgrade and JET *Nucl. Mater. Energy* **12** 111–8
[209] Kallenbach A. *et al* 2020 Developments towards an ELM-free pedestal radiative cooling scenario using noble gas seeding in ASDEX Upgrade *Nucl. Fusion* **61** 016002
[210] Dimitrova M. *et al* 2020 Impact of impurity seeding on the electron energy distribution function in the COMPASS divertor region *Plasma Phys. Control. Fusion* **62** 125015
[211] Petrie T. *et al* 1992 Divertor heat flux reduction by D2 injection in DIII-D *J. Nucl. Mater.* **196–198** 848–53
[212] Petrie T. *et al* 2007 Compatibility of the radiating divertor with high performance plasmas in DIII-D *J. Nucl. Mater.* **363–365** 416–20
[213] Casali L., Eldon D., McLean A., Osborne T., Leonard A., Grierson B. and Ren J. 2022 Impurity leakage and radiative cooling in the first nitrogen and neon seeding study in the closed DIII-D SAS configuration *Nucl. Fusion* **62** 026021
[214] Petrie T. *et al* 2011 First results examining the compatibility of RMP ELM suppression with the radiating divertor in DIII-D *J. Nucl. Mater.* **415** S906–9
[215] McKee G.R. *et al* 2000 Impurity-induced turbulence suppression and reduced transport in the DIII-D tokamak *Phys. Plasmas* **7** 1870–7
[216] Wu D. *et al* 2024 Compatibility of divertor detachment and ELM suppression in DIII-D high-beta plasmas with ITER-similar shape *Nucl. Fusion* **64** 086042
[217] Wang L. *et al* 2021 Integration of full divertor detachment with improved core confinement for tokamak fusion plasmas *Nat. Commun.* **12** 1365
[218] Innocente P., Balbinot L., Bufferand H. and Ciraolo G. 2021 Study of the double null divertor configuration in DTT *Nucl. Mater. Energy* **27** 100985
[219] Ding R. *et al* 2022 Control of tungsten impurity source and edge transport using different gas injection with full tungsten divertor on EAST *Nucl. Mater. Energy* **33** 101250
[220] Wang L. *et al* 2019 Advances in plasma–wall interaction control for H-mode operation over 100 s with ITER-like tungsten divertor on EAST *Nucl. Fusion* **59** 086036
[221] Eldon D. *et al* 2021 An analysis of controlled detachment by seeding various impurity species in high performance scenarios on DIII-D and EAST *Nucl. Mater. Energy* **27** 100963
[222] Xiang L., Militello F., Moulton D., Subba F., Aho-Mantila L., Coster D., Wensing M., Lunt T., Wischmeier M. and Reimerdes H. 2021 The operational space for divertor power exhaust in DEMO with a Super-X divertor *Nucl. Fusion* **61** 076007
[223] Sorokina D., Senichenkov I., Vekshina E. and Rozhansky V. 2018 Testing of the SOLPS-ITER code at Globus-M2 spherical tokamak with detached divertor *MATEC Web of Conf.* vol 245 (EDP Sciences) p 13003
[224] Zhang Y., Sang C., Li J., Zheng G., Senichenkov I.Y., Rozhansky V.A., Zhang C., Wang Y., Zhao X. and Wang D. 2022 Modeling of the effects of impurity seeding on plasma detachment and impurity screening of snowflake divertor on HL-2M tokamak by SOLPS-ITER *Nucl. Fusion* **62** 106006
[225] Glöggler S. *et al* 2019 Characterisation of highly radiating neon seeded plasmas in JET-ILW *Nucl. Fusion* **59** 126031
[226] Telesca G., Ivanova-Stanik I., Zagórski R., Brezinsek S., Czarnecka A., Drewelow P., Giroud C., Huber A., Wiesen S. and Wischmeier M. 2017 High power neon seeded JET discharges: experiments and simulations *Nucl. Mater. Energy* **12** 882–6
[227] Telesca G., Ivanova-Stanik I., Zagorski R., Brezinsek S., Czarnecka A., Drewelow P., Giroud C., Marsen S. and Wischmeier M. 2015 Numerical simulations of JET discharges with the ITER-like wall for different nitrogen seeding scenarios *J. Nucl. Mater.* **463** 577–81
[228] Maddison G. *et al* 2009 Impurity-seeding experiments on JET in preparation for the ITER-like wall *36th EPS Conf. on Plasma Physics* (*Sofia, Bulgaria, 29 June–3 July 2009*) (European Physical Society) (https://pure.mpg.de/pubman/faces/ViewItemOverviewPage.jsp?itemId = item_2141788_3)
[229] Huber A. *et al* 2014 Impact of strong impurity seeding on the radiation losses in JET with ITER-like wall *41st EPS Conf. on Plasma Physics* (*Berlin, Germany, 22–26 June 2014*) (https://cris.vtt.fi/en/publications/impact-of-strong-impurity-seeding-on-the-radiation-losses-in-jet-)
[230] Zagórski R., Ivanova-Stanik I., Czarnecka A., Telesca G. and Brezinsek S. 2015 Influence of seeding and SOL transport on plasma parameters in JET ITER-like wall H-mode discharges *J. Nucl. Mater.* **463** 649–53
[231] Maddison G. *et al* 2011 Moderation of target loads using fuelling and impurity seeding on JET *J. Nucl. Mater.* **415** S313–7
[232] Huber A. *et al* 2020 Peculiarity of highly radiating multi-impurity seeded H-mode plasmas on JET with ITER-like wall *Phys. Scr.* **2020** 014055
[233] Yamoto S., Hoshino K., Homma Y., Nakano T. and Hayashi N. 2023 Transient analysis of high-Z impurity screening by additional injection of low-Z impurity using integrated divertor code SONIC *Nucl. Fusion* **63** 076019
[234] Gupta A. *et al* 2025 Detachment control in KSTAR with tungsten divertor (arXiv:2505.07978)
[235] Masuzaki S. *et al* 2013 Divertor heat and particle control experiments on the large helical device *J. Nucl. Mater.* **438** S133–8
[236] Miyazawa J. *et al* 2005 Self-sustained detachment observed in LHD and comparison with detachment and Marfe in W7-AS *15th Int. Stellerator Workshop (Madrid, 3–7 October 2005* (available at: https://pure.mpg.de/pubman/faces/ViewItemOverviewPage.jsp?itemId = item_2143976)
[237] Myatra O. 2021 Numerical modelling of detached plasmas in the MAST upgrade Super-X divertor *PhD Thesis* University of York (available at: https://etheses.whiterose.ac.uk/29424/)
[238] Verhaegh K. *et al* 2021 A novel hydrogenic spectroscopic technique for inferring the role of plasma–molecule interaction on power and particle balance during detached conditions *Plasma Phys. Control. Fusion* **63** 035018

[239] Soukhanovskii V. *et al* 2006 Divertor heat flux reduction and detachment in NSTX *IAEA FEC* (*Chengdu, China, 16–22 October 2006*) (available at: https://www-pub.iaea.org/MTCD/Meetings/FEC2006/ex_p4-28.pdf)
[240] Soukhanovskii V.A. *et al* 2009 Divertor heat flux mitigation in the National Spherical Torus Experiment *Phys. Plasmas* **16** 022501
[241] Osawa R., Moulton D., Newton S.L., Henderson S.S., Lipschultz B. and Hudoba A. 2023 SOLPS-ITER analysis of a proposed STEP double null geometry: impact of the degree of disconnection on power-sharing *Nucl. Fusion* **63** 076032
[242] Theiler C. *et al* 2018 SOL transport and detachment in alternative divertor configurations in TCV L-and H-mode plasmas *27th IAEA Fusion Energy Conf. (FEC 2018)* (*Gandhinagar, India, 22–27 October 2018*) (available at: https://inis.iaea.org/records/wmd42-kyd46)
[243] Smolders A. *et al* 2020 Comparison of high density and nitrogen seeded detachment using SOLPS-ITER simulations of the tokamak á configuration variable *Plasma Phys. Control. Fusion* **62** 125006
[244] Stagni A. *et al* 2022 Dependence of scrape-off layer profiles and turbulence on gas fuelling in high density H-mode regimes in TCV *Nucl. Fusion* **62** 096031
[245] Takimoto T., Ishikawa F., Iijima T., Tonegawa A., Sato K. and Kawamura K. 2017 Experimental simulation of the Super-X divertor for detached plasma using TPD-Sheet IV *Fusion Eng. Des.* **124** 235–8
[246] Effenberg F. *et al* 2018 Demonstration of power exhaust control by impurity seeding in the island divertor at Wendelstein 7-X *Preprint: 2018 IAEA Fusion Energy Conf. (Gandhinagar [EX/9-2])*
[247] Maget P. *et al* 2021 How nitrogen seeding securizes plasma ramp-up in the metallic environment of WEST *47th European Physical Society Virtual Conf.* (*Online, 21–25 June 2021*) (available at: https://shs.hal.science/OPENAIRE/cea-03300676v1)